February 2022

Ph.D. Dissertation

Synthesis and Applications of Perovskite Thin Layers with Aqueous Precursor

Graduate School of Chosun University

Department of Chemistry

Zobia Irshad

Synthesis and Applications of Perovskite Thin Layers with Aqueous Precursor

수용액을 이용한 페로브스카이트 박막 제조 및 응용

February 25, 2022

Graduate School of Chosun University

Department of Chemistry

Zobia Irshad

Synthesis and Applications of Perovskite Thin Layers with Aqeous Precursor

Advisor: Prof. Jae Kwan Lee

This dissertation is submitted to the Graduate School of Chosun University in partial fulfillment of the requirements for the degree of Doctor of Philosophy in Science

October 2021

Graduate School of Chosun University

Department of Chemistry

Zobia Irshad

This is to certify that the Ph.D. dissertation of Zobia Irshad has successfully met the dissertation requirements of Chosun University.

위원장	조선대학교 교수	김 호 중 (인)
위 원	조선대학교 교수	손 홍 래 (인)
위 원	조선대학교 교수	이 재 관 (인)
위 원	조선대학교 교수	김 선 우 (인)
위 원	전남대학교 교수	김 용 인 (인)

January 2022

Graduate School of Chosun University

CONTENTS

I. CHAPTER 1 - INTRODUCTION

II. CHAPTER 2

III. CHAPTER 3

III. CHAPTER 4

ABBREVIATIONS

PV:	Photovoltaic PCE: power conversion efficiency
VOC:	Open-circuit voltage JSC short-circuit current density
FF:	Fill factor DSSC: dye-sensitized solar cell
ETL:	Electron-transporting layer
HTL:	Hole-transporting layer
MA:	Methylammonium
FA:	Formamidinium
FTO:	Fluorine-doped tin oxide NC: nanocrystal
HTM:	Hole-transporting material
FWHM:	Full width at half maximum
PL:	Photoluminescence
DMF:	N,N-dimethylformamide
DMSO:	Dimethyl sulfoxide
CB:	Conduction band
VB:	Valence band
XRD:	X-ray diffraction
AFM:	Atomic force microscopy
TEM:	Transmission electron microscopy
XPS:	X-ray photoelectron spectroscopy
EF:	Fermi level
Eg:	Band-gap
q:	Elementary charg

LIST OF FIGURES

CHAPTER 1

CHAPTER 2

CHAPTER 3

CHAPTER 4

Abstract

Synthesis and Applications of Perovskite Thin Layers with Aqueous Precursor

Zobia Irshad

Advisor: Prof Jae Kwan Lee

Department of Chemistry

Graduate School of Chosun University

Perovskite solar cells (PSC) performance has increased speedily in the past years and recent record having power conversion efficiency (PCE) of 25.6%. This has achieved a lot of concentration towards this alternative PSC that can be fabricated with non-toxic materials than traditional silicon solar cells. Thus, perovskite-based photovoltaics have some common issues to reach reliable and stable commercialization, including the need to identify fabrication processes that can yield optimal material parameters for better photovoltaic performance. In principally the low defect density, the excellent crystallinity and uniformity coverage of perovskite materials, especially alkylammonium lead halide $(RNH_3)PbX_3$, on the cells are critical for improving the PCEs of the PrSCs devices. Nevertheless, PrSCs have small active areas for fabrication and experienced from the substrate size limitation due to spin-casting approaches. In this work, we successfully demonstrated the all-dip-coating deposition of an efficient FAPbI3 and $MA_xFA_{1-x}PbI_3$ perovskite layers from an aqueous halide-free lead precursor as a simple, low-cost and an

environmentally benign method. We have also modulated the phase and surface crystallinity of FAPbI3 and $MA_xFA_{1-x}PbI_3$ perovskites from all sequential-dip-coating approach to fabricate an efficient PSCs device. It is study that this all-dip-coating process might add a good significance to the development and the fascinating deposition technology with superior crystallinity, morphology and surface coverages of perovskite film to dominate the spin-coating strategy which has a size restriction and the use of very toxic and detrimental organic solvents for highly performing PrSCs. which might be a helpful for the commercialization of PrSCs. Similarly, the $MAPbI_3$ or various mixed halide perovskites deposited by a aqueous $Pb(NO_3)_2$ may experiences additional ion-exchange reactions with un-reacted $Pb(NO_3)_2$, still in the solid phase, converting into the yellow PbI_2. We believe that by optimized all sequential dipping conditions might add more significance to the development of more fascinate deposition technology to overcome the well-established spin-casting approach limiting substrate size and the usage of toxic and detrimental organic solvents.

Abstract(국문)

수용액을 이용한 페로브스카이트 박막 제조 및 응용

Zobia Irshad

Advisor: Prof Jae Kwan Lee

Department of Chemistry

Graduate School of Chosun University

페로브스카이트 태양전지는 지난 몇 년간 매우 빠른 속도록 성장해오고 있고, 25.6%에 달하는 광전변환효율을 기록하고 있다. 이는 기존 실리콘 태양전지를 대체할 새로운 태양전지로 부상하며 많은 기술 역량이 집중되고 있다. 이를 위해, 상용화에 필요한 프로세스의 안정성과 신뢰성 확보를 위한 다양한 노력이 수행되어 왔으며 페로브스카이트 태양전지의 성능 개선을 위한 최적의 소재 특성을 구현하는 제조 공정 개발도 병행되고 있다. 알킬암모늄 할로젠화납, $(RNH_3)PbX_3$과 같은 페로브스카이트 소재 박막의 낮은 결함 밀

도와 우수한 결정성 및 균일한 커버리지 등은 페로브스카이트 태양전지의 광전변환효율을 향샹시킬 수 있는 핵심 요소이다. 현재 페로브스카이트 소재는 할로젠화납, PbX_2 전구체를 이용하고 있지만 DMF, DMSO와 같은 독성 유기용매에 주로 용해되는 문제가 있다. 또한 이들의 박막의 제조는 스핀코팅방법이 적용되고 있으며, 이는 대면적 박막 제조를 위해서는 많은 문제점을 가지고 있다. 본 학위논문 연구에서는 페로브스카이트 소재 박막을 제조함에 있어, 스핀코팅 방법이 아니 딥코팅 방법을 적용하였고, 할로젠을 함유하고 있지 않은 수용액에 용해된 납전구체를 이용해 환경친화적이고 인체무해한 효율적의 제조공정 개발을 통해 고성능 $FAPbI_3$ 와 $MA_xFA_{1-x}PbI_3$ 페로브스카이트 박막을 제조하는 연구를 성공적으로 수행하였다. 다양한 조건 변화를 통해 $FAPbI_3$ 와 $MA_xFA_{1-x}PbI_3$ 페로브스카이트 결정상과 결정구조를 조절하였고, 박막제조 전공정을 딥코팅 방법을 적용하고자 하였다. 본 연구를 통해 스핀코팅 방법을 적용한 페로브스카이트 박막 성능과 비교될 수 있는 우수한 페로브스카이트 박막의 몰폴로지와 결정성 그리고 표면 커버리지를

구현할 수 있었다. 이러한 연구과정에서 Successive Solid-State Ion-Exchange and Reaction (SSIER)의 새로운 제조공정을 적용해 수용액 전구체인 Pb(NO3)2로부터 다양한 페로브스카이트 구조와 박막을 제조하였고, 이를 페로브스카이트 태양전지에 응용하여 우수한 태양전지 광전변환 효율을 도출하였다. 본 학위논문은 환경친화적인 페로브스카이트 소재 박막의 대면적 제조를 손쉽게 적용할 수 있는 독창적이고 우수한 연구결과와 이를 응용한 태양전지 성능을 향상시키는 연구를 수행하는 유의미한 결과를 제시하고 있다.

Chapter 1 – Introduction

Background

1.1 World Energy Consumption and Energy Crisis

Energy is in the main part of human development and its existence. Energy mostly depended on the progress of men development. The development of any country depends upon the amount of energy used per capita. In 2015 42% energy used by United states of America and China together by the whole world. Nonetheless, united states of America had only 4.5% of entire world's inhabitants [1]. The total energy utilization involves energy source from every scientific area among all the countries instead of energy obtained from food and biomass consumption [2]. The most difficult part is that with the progress of men civilization there is a endless growth in necessity of energy. The non-sustainable energy resources are usually oil, natural gas, coal have limited aptitude. Most of them have intensive effect on atmosphere. Thus, it is necessary to work on sustainable and causes less environmental resource. The only solution of this problem is to utilized the Renewable energy sources even though the budgets of utilizing energy from these sources are still very expensive

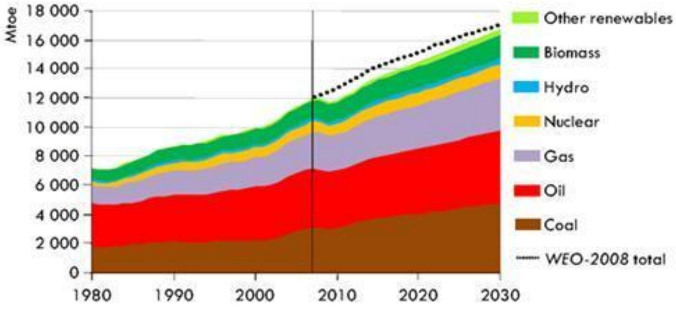

Figure 1: Worlds energy consumption map

1.2 Renewable Energy Consumption

In 2012 81% was the world's total energy consumption came from combination of non-renewable sources of energy such as petroleum, coal, natural gas and nuclear energy. about 19% of rom renewable sources of energy. The need of obtained energy from these non-renewable sources is that they are cost effective. They can easily supply from one place to another. However, the majority of resources are not at all environment friendly. The burning of coal making atmosphere more toxic and pollutant. [4]. Likewise, we have limited capacity of these non-renewable sources of energy if we used without any calculation it will finished very soon. So, that why renewable sources of energy become a main targeted work day-by-day. There are numerous resources of non-renewable energy (wind, sunlight, tides, waves, geothermal heat etc). There is a quick growth in dimensions of various types of renewable energy sources [5]. While hydro and wind power sources rule over the world during the primary years, whereas the solar PV renewable energy is growing up in terms of capacity very quickly.

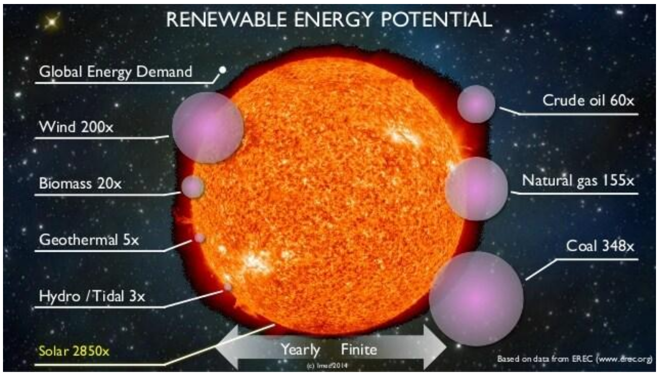

Figure 2: Renewable energy consumption report

1.3 Solar Energy and solar radiation

Solar energy originates from the sun and reached to earth in the form of electromagnetic rays. While very small amount of energy hits the earth, that can be sufficient to achieve the energy prerequisite of mankind. The most marvelous sources of renewable energy is Solar energy and have previously displayed a great potential to be a prime source of energy in the future. The benefits of solar energy are:

- Solar energy is plentiful in landscape.
- Solae energy is frequently ecologically friendly.
- The upholding cost of solar panels is moderately very little.
- This technology is noise free.
- It offers a very trustworthy source of energy.
- Solar power also offers energy safety.
- Solar energy is also come in sustainable energy resource

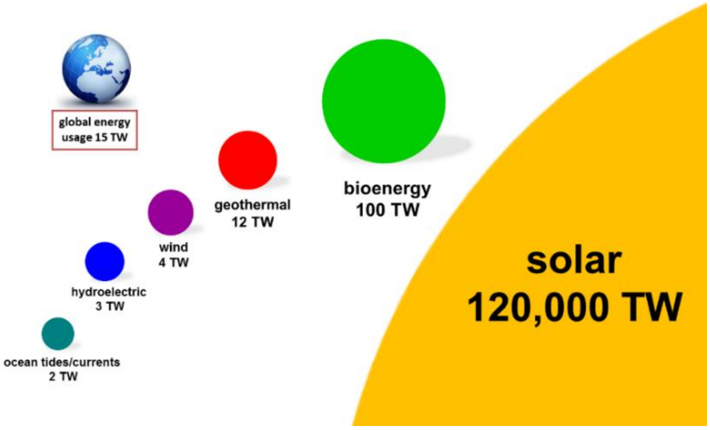

Figure 3: Global energy capacity

Figure 3 displays the actual potential of solar energy opposed to other resources. We get the 2300 TW/year potential power which achieved from solar devices it helps to compared with other sources of energy. The total power utilized by the human is nearly 16 TW/year. Consequently, efficient abstraction of solar energy can help to accomplish all the energy requirement for manhood. Nonetheless the real image concerning the fraction of energy used from another sources in 2014 has been described in figure 3 It displays that around 76% of entire energy used from non-renewable sources and the remainder 24% was arriving from renewable energy. If we examine the collapse of this 24% from renewable energy resources, we can understand that only near 1.2% was approaching from Solar PV [7] Nonetheless the hopeful symbol for Solar PV is that the cost per unit power is decreased potentially upon the years (Figure 4) [9]. Figure 4 explained the contrast of solar technology with others resource if work on this research upto 2030 then we can believe that the future is depend upon the solar photovoltaics just because of its outstanding results, and significant effect on economy and the environment, respectively

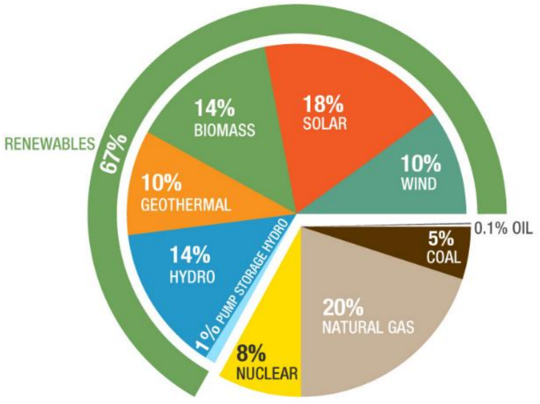

Figure 4: Renewable energy consumption in 2020

1.4 Introduction to Solar Cell Devices

Solar cell is a device which used to convert solar energy into electrical energy. The basic structure of the solar cell device is displayed in the Figure 5. Which present the working principles of the solar cell-light tempting into the active layer, holes and electrons producing and then move across the transporting layer and finally assembly at the conductor, generate the photo current

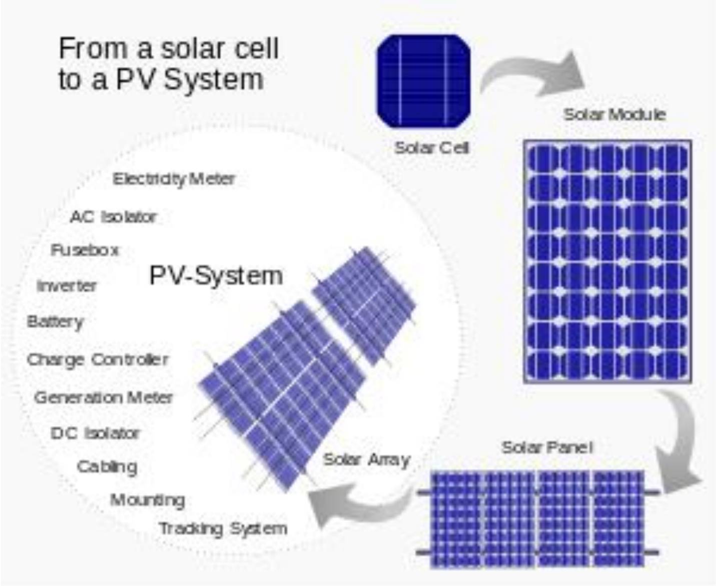

Figure .5. Solar cell devices

1.5 Perovskite Solar Cells

A perovskite solar cell (PSC) is a sort of solar cell which consist of perovskite-structured material, mostly consist of a hybrid organic-inorganic lead or tin halide-based compound, act as the active layer [12] Perovskite materials, such as methylammonium lead halides and all-inorganic cesium lead halide, are easily synthesis and cost effective.

The Solar cell device PCE efficiently increased from 3.8% in 2009[4] to 25.5%

in 2020 through single-junction designs, and, get silicon-based tandem cells, to 29.15%, PCE [11] go beyond the maximum efficiency attained in single-junction silicon solar device. Perovskite solar cells come in the fastest-advancing solar technology as of last years. [9] the perovskite solar cells gain commercial and ecological attention due to their potential of accomplishing even higher efficiencies and very low manufacture costs. The main problem that perovskite cell faced is the short-term stability

Perovskite solar cells fulfilled the main two conditions. Low material cost, fabrication of material is very easy and simple roll-to-roll handing out makes perovskite solar cells very stimulating alternative. Likewise, there are many other groups previously reported to have power conversion efficiencies more than 20% [10]. Figure 6 displays the power conversion efficiency development of perovskite solar devices associated with further solar technologies**.**

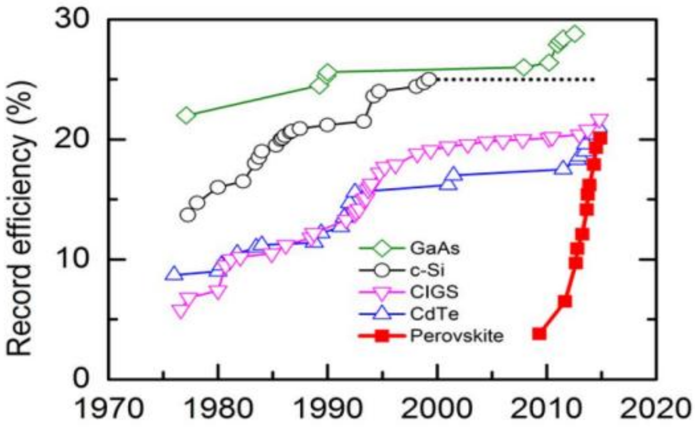

Figure 6: Evolution of power conversion efficiency of perovskite solar cells compared with other solar technologie

1.5.1 Working mechanisms and development

Solar cells structure mostly consist of an N-type semiconductor and a P-type semiconductor. When the solar light is hits surface of active layer in the device, it can generate two parts-electrons and holes. Then the electrons having negative charged ion move toward the N-type semiconductors (also known acceptor) and accumulated around the cathode whereas holes with positive charge moved toward the P-type semiconductor (donor) finally collect around the anode. When we induce the external circuit, the current streams move between the cathode and the anode. In this way photocurrent generates. Figure (7) is explain of the generation of photocurrent.

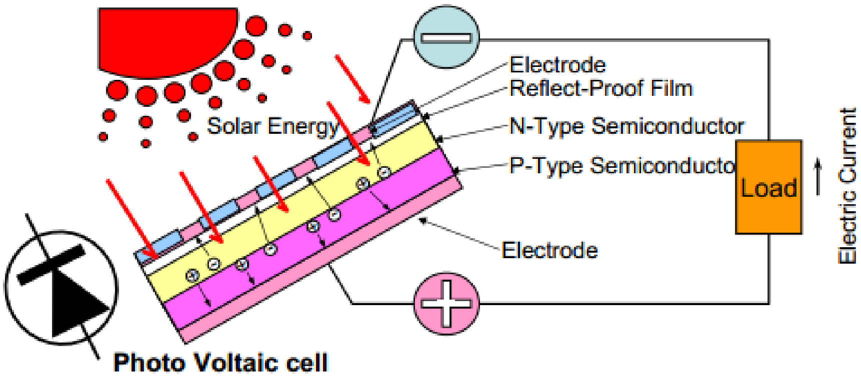

Figure 7. Basic working mechanisms of solar cell device.

Traditional silicon solar cell shows the restricted growth just because of its high cost in the silicon refining processing and pollution matter. In the meantime, polymer solar cells, is become the significant choice for the solar cell device, even it does not achieve the highest PCE. In last years, the methyl ammonium lead halide perovskite (CH3NH3PbI3) compounds act as more competent because of their excellent optical and has large light absorption coefficient (5.7×104 cm−1 at 600 nm)[11-12], high charge carrier mobility (hole transfer speed of 164 cm 2 V -1 S -1 and electron transfer speed 24 cm2V -1 S -1 for MAPbI3 perovskite)[13], long charge diffusion length (~100nm)[14,15], simple fabrication approaches (solution-processing) etc. The above figures display the basic working methodology of the perovskite layer and the progress of perovskite solar cells opposed to remaining solar cells. the perovskite solar cell act as the active layer (also called light absorbing layer) Figure 7. Charge carriers then move from (HTL) and (ETL), accumulate at the corresponding electrode, generate the photocurrent. This is basic mechanism of perovskite solar cells word. Last year's research report explain, perovskite solar cells shows huge improving in the efficiency which show that perovskite become a very significant material in photovoltaic field. [16]

1.5.2 Component and properties of perovskite

The perovskite chemical structure usually based on the CH3NH3PbX3 (X=Cl, Br, I or their mixture). The name perovskite obtained from CaTiO3, in 19th century. discovered by a Russian Mineralogist. After the finding, the definition of perovskite has changed. In 1991, German scientist David Mitzi firstly introduced perovskite compound in organic photovoltaics (OPV) field. [17] There are three main perovskite crystal structures-cubic, tetragonal and orthorhombic. The crystal structures are exposed in the below figure.

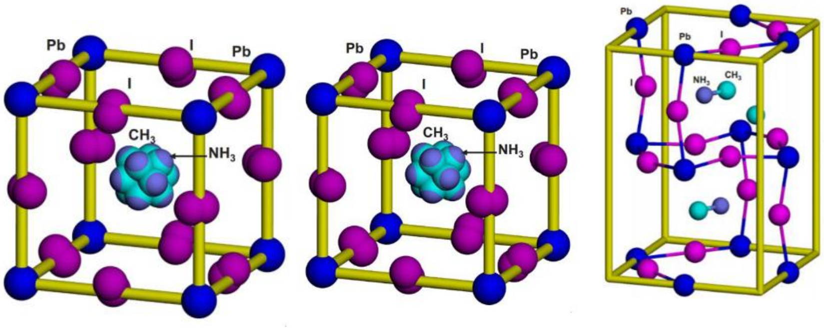

(a) Cubic structure **(b)** Tetragonal structure **(c)** Orthorhombic structure

Figure. 8. Perovskite crystal structures

Geometric tolerance factor (t) was explained by a unit of researchers in 1927. The formability of perovskite was estimated based on t value [23].

$$t = (rA + rM)/\sqrt{2}(rM + rX)$$

Eqn 2.2.1 where rA, rM and rX were the effective ionic radii for A, M and X ions, respectively. Based on effective ionic radii, the rA in APbX3 (X=Cl, Br, I) perovskite was calculated to be t=0.8 to t=124. Cations with radii between 1.60Å and 2.5Å were found to form perovskite structures. Therefore, methylammonium cation is significant for lead halide perovskite because its ionic radius is 1.8Å. Since the tolerance factor of CH3NH3PbI3 was calculated as 0.83, mild deviation from an ideal cubic structure was expected [24-25] The information of optical u properties helps in study of the electronic structures of perovskite materials and therefore further enhance the device performances. Many researches have been carried out on both thin films [26-27] and single crystals [28]. The initial interest focused on methylammonium

(MA) lead trihalide ($CH_3NH_3PbX_3$, where X is halide, have optical band gap of 1.5 to 2.3eV, it is significant to notify that recent progresses are transferring attention towards formamidinum ($HC(NH_2)_2PbI_3$ or "FA") lead tri-halide. Most effective perovskite devices were fabricated using a mixture of $FAPbI_3$ and $MAPbBr_3$. Perovskite lattice forms three phases (orthorhombic, tetragonal and cubic) at different temperatures. All the perovskites of photovoltaic interest tend to produce less symmetric orthorhombic structure at lower temperature whilst the increase in temperature will shift the phase towards more symmetrical arrangements, until the symmetrical cubic structure is made. It is observed that more than two phase transitions is likely to happen in the process [28-30]. During the geometry transition from tetragonal to cubic, both band-gaps of $CH_3NH_3PbI_3$ and C $CH_3NH_3PbBr_3$ and binding energies remain unchanged. While these parameters alter when phase transfer happens from orthorhombic to tetragonal [35]. For the case of $CH_3NH_3PbBr_3$, the phase transition from cubic to tetragonal undergoes at circa 330.4 K, while for the case of $CH_3NH_3PbBr_3$, it happens at 154.0 K. $CH_3NH_3PbBr_3$ crystallizes an orthorhombic structure below approximately 161.4 K, but $CH_3NH_3PbBr_3$ requires temperature down to 148.8 K to generate an orthorhombic geometry [31-34].

1.6 Working Mechanism of Photovoltaic Devices

In perovskite solar cells, Figure 8, the perovskite material operates as a semiconductor light absorbing layer which allows non-polar transport of photo-generated carriers that are selectively conducted by charge transport layers to the corresponding electrodes [38-39]

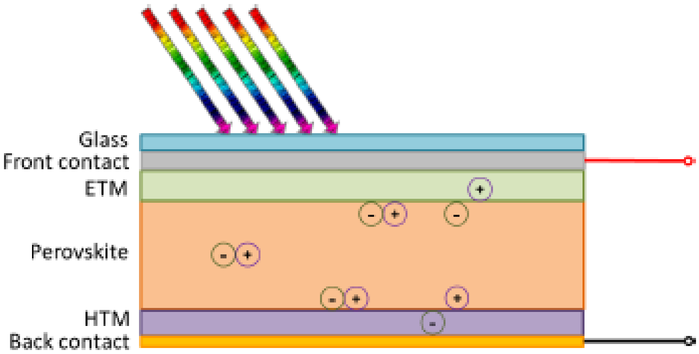

Figure.9 Schematic diagram of the working mechanism of a perovskite solar cell**.**

The perovskite performance depends upon the limited no of factors. Commonly, they are divided into two types: structure and material characteristics. Primary, choice the planar or mesoporous structure, conventional or inverted configuration formerly selecting the material (for ETM and HTM), which is also very important part of device performance. The suitable selection of ETM and HTM leads to ideal band alignment, which improved charge transportation. furthermore, the layer thicknesses also influence the cell performance, film that is too thin have face different problems such as less light harvesting and non-uniform surface coverage; film that is too thick frequently caused rise in series resistance or lesser voltage if the film quality is not significant. The material properties, the deposition technique and post treatments alter the crystallinity, electrical and optical characterizations of the compound, which disturbed the device performance. Also, the quantity of additive [40-42] for both charge transport compounds and perovskite material is crucial to the solar cell performance.

1.7 Deposition Approach

1.7.1 One-step solution process

The Miyasaka et al introduced first time One-step spin-coating method (Figure 9) by using the CH_3NH_3X and PbX_2 were mixed in DMF with 1:1 molar ratio at controlled temperature (e.g. 90^0 C) into photovoltaic community [48]. They introduced Precursor solution of perovskite through spin-casting onto the surface of the substrate followed by solvent drying. The main benefit of this technique is less time consuming and appropriate for entire perovskite fabrication by various lead resources. Nevertheless, due to persisted precipitation of perovskite material, usually one-step spin-coating leads incomplete coverage resulting poor morphological of film, yielding ineffective photovoltaic device performances and low-slung reproducibility. [45-46]

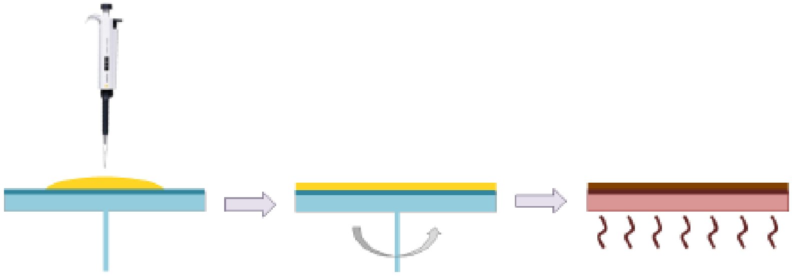

Figure. 10. Schematic diagram of one-step spin-coating deposition method

1.7.2 Sequential process

To reduce the drawbacks of one-step spin-coating method, Gratzel et al. introduced a sequential deposition technique [50]. The schematic diagram displays in Figure 10. first of all, spin -coating the PbI_2 solution on the substrate after that dipping into perovskite precursor solution followed by annealed for a certain time; the alter of color of the film shows the formation of perovskite layer in the solution. In the last step removed the solvent through annealing process and permit the grains grow uniformly and effectively. whereas, the two-step deposition method was probable to be predominantly effective for formation organic-inorganic films, in which the organic and inorganic materials had opposing solubility properties. From this method we achieved uniform distributed perovskite films. Nevertheless, the incomplete reaction in CH_3NH_3I solution leads the small grains and rough surface morphology [51-53]. Therefore, thicker HTM was needed to avoid shunting. This increase series resistance, and affect the device performance. Also, it was valuable observing that the sequential deposition was frequently achieve high efficiency due to nanostructured TiO_2 scaffolds, but was rarely stated to be appropriate for fabricating planar structure devices. [54]

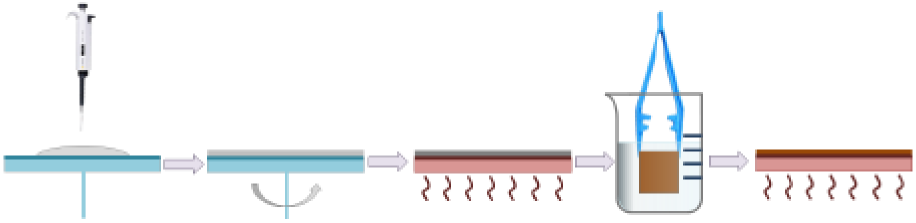

Figure.11. Schematic diagram of sequential deposition method

1.7.3 Dual-source evaporation method

The novel dual source evaporation method used to achieve smooth film and uniform coverage, (Figure 11) was introduced by Snaith and co-workers [56-57]. This vacuum evaporation was significantly achieved high-performance devices through thin films of perovskite under control condition. Though, this evaporation deposition technique needs high vacuum chamber and it takes a long time due to low evaporation rate, this approaches costly for commercial production.

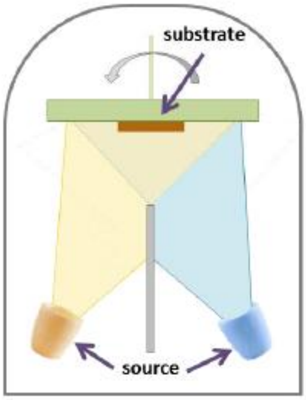

Figure.12. Schematic diagram of dual-source evaporation deposition method

1.7.4 Vapor-assisted solution process (VASP)

Additional two-step deposition technique was given by Yang et al [36] that is of analogous to the first step of sequential procedure. As show in Figure 12, PbI_2 was spin casting on substrate further drying through annealing, as an alternative of dipping substrates into perovskite solution, the layer was then bringing to hot CH3NH3I vapor, and perovskite layer was fabricated in the closed chamber, usually used glassy petri-dish [57]. Over time, pre-deposited PbI2 was converted to perovskite film entirely; isopropanol was used to remove the excessive CH3NH3I residuals on the film surface followed by annealing under nitrogen stream.

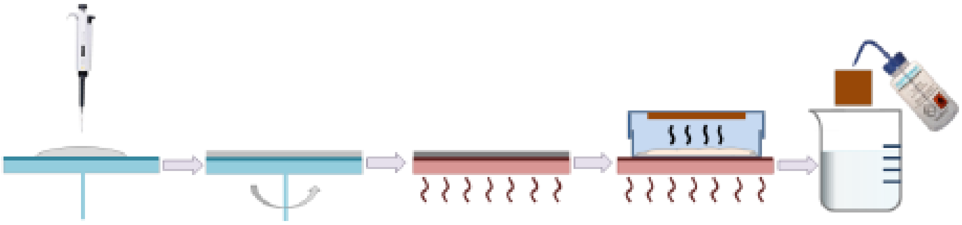

Figure. 13. Schematic diagram of vapor-assisted solution process

1.7.5 Other deposition methods

There are many other deposition approaches were used to attain perfect films for device fabrications and performance. Main factor to introduced suitable substitute of the lead or halide source. Snaith et al introduced Chloride substitution into the precursor solution [58]. This method formed a uniform crystallization to get fully covered layered. The same group using lead acetate as the lead source to obtain ultra-smooth morphology [59]. Monash University researchers reported a fast-crystallization a one-step solution process to achieved perovskite film with superior quality, they using an anti-solvent or Argon stream through the spin-casting step, to eliminate solvent residuals from the precursor solution quickly. This technique influences the perovskite grain growth and dynamics of nucleation to obtained a high-quality and high reproducibility perovskite layer. MAPbBr3 was introduced into FAPbI3 film to stabilize the perovskite phase of FAPbI3[60] Currently, the same group verified an intramolecular exchange idea which complex FAPbI3 crystallization by the direct intramolecular exchange of (DMSO) molecules introducing in PbI2 with formamidinum iodide. This technique influenced the crystallographic orientation of geometry. Large, uniform and packed grains deprived of PbI2 residual could be fictional by this technique to obtained a thin layer with minor surface unevenness. [61-63]

1.8 The optimistic opportunity for perovskite solar cells

The measured band-gap of MAPbI3 perovskite is ～1.5 eV, shows absorption onset at 800 nm, over the entire wavelength range of visible light which made it significant absorber. The high absorption co-efficient of 1:5 104 cm^{-1} and 0:5 104 cm^{-1} at 550 nm and 700 nm respectively permits significant absorption even with use of small thickness film [29]. And the high carrier transport ～8 cm^{2} V^{-1} s^{-1} for MAPbI3 [64]) along with long carrier diffusion length (ranging from 100 nm to 1,000 nm [65]). These reduce the chance of possibility of recombination within the bulk.

Archetypally, perovskite solar cells used n-i-p or p-i-n junction configuration in which a perovskite layer (intrinsic semiconductor layer) is sandwiched among an n-type ETL, such as TiO2 or PCBM) and a p-type HTL, usually spiro-OMeTAD, NiOx or PEDOT: PSS). The energy level alignment as exposed in Fig. 15 is favorable for charge departure [32]. After excitation, the photoelectrons can be fast infused into the conduction band of TiO2, whereas holes are moved toward spiro-OMeTAD. In this way the charges moved in opposite direction and recombination can be eased.

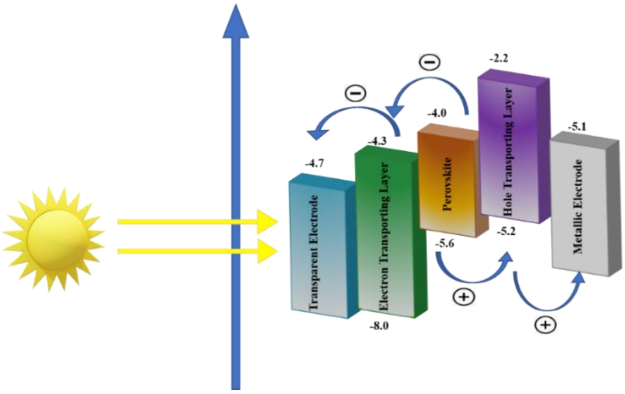

Figure 14: Energy level diagram of perovskite solar cell

The high-quality perovskite films produced through, both one-step and two-step method which are simple, low energy-consuming and efficient other methods such as Roll-to-roll procedures such as spray-coating and blade-coating also help in the fabrication of devices effortless to scale up. These perovskite devices have a short energy payback time (EPBT, defined as the ratio of the total primary energy consumption to the annual electricity generation), which is around 0.3 years, much shorter than silicon-based devices. [66].

The fast progress of perovskite solar cells has flashed the expectation of their functional application. Dar and Gr¨atzel used CuSCN as HTMs for perovskite device [67], which obtained stabilized PCEs above 20%. By introducing a concentrated graphene oxide interlayer among the CuSCN and metal layers, 95% efficiency of the device was effectively stable after 1000 hours aging at 60℃ obtained the maximum power point [68]

Moreover, there are many other industrial corporations all over the world enthusiastic to the commercialization of the perovskite technology. Optimistically, perovskite solar cells will bargain their requests in the future.

1.9 Issues faced by perovskite devices

organometallic halide perovskite based solar devices have revealed numerous astonishing characteristics and efficent efficiency, there are still many on large-scale application.

1.9.1 Hysteresis issues

Hysteresis is a factor usually detected during the performance tests of perovskite devices. [69-70]. The current-voltage curve shows declining voltage (reverse scan) have higher currents per voltage than forward scan.

These devices show overestimated performance of perovskite devices. Several factors have been observed dye to this condition, together with trap states [70], Ferro electricity [71, 22] and ion migration [73–76]. The significant progress is still required for improved understanding and the evasion of hysteresis. Hysteresis is more effective in planar devices than in mesoporous solar cells, and powerfully reliant on the scan speed, light-soaking and pre-biasing circumstances [77-80], annealing [81], perovskite crystal growth [86-88]. For the precise measurement of perovskite devices, it is usually needed to measure both forward and reverse J-V curves at numerous scan rates.

1.9.2 Stability

Stability is probably the biggest encounter for the installment of perovskite device. the decomposition reaction

$$MAPbI_3 \rightleftharpoons PbI_2 + MAI \qquad (2)$$

The change in the Gibbs free energy at 300K is $\Delta G° 300K = 0{:}16$ eV per formula unit [90], shows the perovskite device is stable under standard conditions, nevertheless the minor magnitude proposes the stability is very feeble and can be alter effortlessly, even in the presence of water. Since MAI is soluble in water, the saturation concentration to overcome the decomposition of MAPbI3 is assessed to be as high as ~8 g=L [88], The minor amount of humidity cause serious decomposition of the perovskite film. Also, further decomposition followed by reaction 1.4 which further improved by oxygen or UV light due to the consumption of the HI [84] through the reactions presented in Equation 1.5 and Equation 1.6, respectively. It was observed that MAPbI3 would be decomposed into PbI2 after 18 h contact with a 60% humidity at 35℃ [84]. As a consequence, optimized device architecture encapsulation for the long-term stability of perovskite solar cells.

$$\text{MAI (aq)} \rightleftharpoons \text{CH}_3\text{NH}_2\text{ (aq)} + \text{HI (aq)} \qquad (3)$$

$$4\text{HI (aq)} + \text{O}_2\text{ (g)} \rightleftharpoons 2\text{I}_2\text{ (s)} + 2\text{H}_2\text{O (l)} \qquad (4)$$

$$2\text{HI (aq)} \rightleftharpoons \text{H}_2\text{ (g)} + \text{I}_2\text{ (s)} \qquad (5)$$

1.9.3 Toxicity

Lead compounds are very hazardous for the environment, and the impact of lead-based perovskite devices on the environment is a big concern for their large-scale application. Several researchers have tried to replace Pb with other less toxic elements such as Sn [85-86]. Though MASnI3 also showed good semi-conductive properties with a band gap of ~1.3 eV, Sn2+ is easily oxidized into Sn4+ which can cause p-type doping to the material [85]. Partial replacement of Pb with Sn has also been investigated to reduce the use of lead [77–79], but the highest PCE so far reported for Sn-Pb alloy-based perovskite solar cell is only 15.2% for MASn0.25Pb0.75I3 [88], and stability is still a problem. So, until now, the most efficient perovskite solar cells still have to be based on lead, but with proper encapsulation and the development of lead recycling processes which is also extremely important for lead acid batteries, the harm of lead content to the environment could be minimized.

Chapter 2 - Experimental Section

Synthesis of Materials

2.1 Synthesis of Methylammonium Iodide

Methylammonium iodide was synthesized by adding hydroiodic acid (30 mL, 0.227 mol, 57 wt.% in water, Aldrich) into methylamine (27.8 mL, 0.273 mol, 40% in methanol, TCI) and stirring at 0℃ for 2 h, the unwanted solvent was evaporated at 50℃ for 1 h and obtained (CH3NH3I) compound. The produced (CH3NH3I) powder was rinsed several times with ethanol, diethyl ether and dried through nitrogen vacuum and used devoid of any further purification.

2.2 Synthesis of Formamidine iodide

Formamidine iodide was obtained by reaction of hydrochloric acid (30 mL, 0.227 mol, 37 wt.% in water, Aldrich) and formamidine acetate (15g) in a round-bottomed flask with continuous stirring at 0 ℃ for 2 h. the resultant solution was vaporized at 50 ℃ for 1 h and produced NH2CH=NH2I (FAI). The obtained FAI powder was wash away three times with ethanol and diethyl ether. Finally dried through vacuum and no need for further purification.

2.3 Synthesis of compact Titanium Oxide (c-TiO_2)

The compact titanium oxide precursor solution was synthesized through reaction of titanium source of 0.152 μL in 1.874 mL of 1-Butanol. Sonicate the resultant solution for 30 minutes. The subsequent solution has a yellow color.

2.4 Synthesis of mesoporous Titanium Oxide (mp-TiO_2)

The mesoporous titanium oxide precursor solution was produced by taking 1.6g of titanium paste of 40 nm size in 10 mL of anhydrous ethanol and stir the solution at least for 12 hrs. maintain room temperature until reaction completion. The resultant mixture has a whitish color.

2.5 Synthesis of Zinc Oxide Sol-Gel Solution (ZnOs-g)

The zinc oxide sol-gel precursor solution was prepared through the reaction of 1.6 g zinc acetate dihydrate, 0.5 g of ethanol amine with dissolved in 10 mL of 2-methoxy ethanol and stir the resultant solution for 13 hrs. Until required compound is obtained.

2.6 Perovskite solar cells device fabrication

The basic procedure was applied for the fabrication of planar heterojunction PSCs and it follows the chronological order as seen bellow.

1. washing of FTO substrate
2. Spin-coating of Compact-TiO_2
3. Spin-coating of mesoporous -TiO_2
4. Spin-coating of ZnO Sol-Gel.
5. Dip-coating fabrication of $Pb(NO_3)_2$ layer.
6. Dip-Coating fabrication of perovskite layer.
7. Spin-coating of spiro-OMeTAD
8. Thermal evaporation of MoO_3
9. Thermal evaporation of Ag/Au

The glass substrates fluorine doped tin oxide (FTO) were bought from the corporation Thin film devices Inc. and were in squares of 15×15 mm^2. The 75 %

of the glass substrates surface covered by FTO and a sheet resistance of 7 Ω/sq.

2.7 Cleaning of FTO substrates

It is essential to clean FTO/glass substrates before the fabrication of different layer can commerce, even a tiny dust particle on the substrate will disturb the final cells performance. This was completed in just five steps. From First to fourth step cleaning was done under ultrasonic bath for about 30 min. The ultrasonic bath based on high frequency waves that make cavitation bubbles that helps to eliminate contaminations on the substrates. In each step the substrates were kept in a new beaker to diminish the mixing of solvents. The initial cleaning step was made with detergent dissolved in deionized water. in second cleaning step wash substrate with deionized water, third step was followed with absolute ethanol and fourth rinsed with acetone. After that substrates were pick up one by one from the beaker and blow dry before placed to dry in oven to minimize left over solution on substrates. The last step is drying process in which substrate was kept in in oven at 120 ℃ for minimum 2 h. .

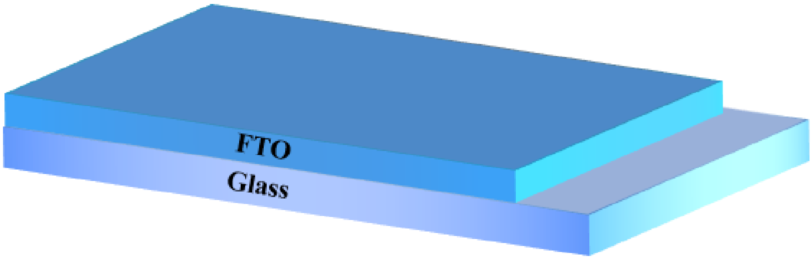

Figure 1: Schematic figure of the cleaned glass/FTO substrate

Figure 18 above shows the layers that been cleaned by all above steps and how much approximately the FTO covers the glass surface.

2.8 Preparation of compact TiO_2 (c-TiO_2) layer by spin-casting

The cleaned FTO/glass substrate were placed under UV-ozone treated just for 10 minutes followed by masking to keep some of the FTO permitted from TiO_2, didn’t block the electrode area. The definite programmer was set in spin-coater machine for the deposition of c-TiO_2 layer. After fabrication of c-TiO_2 film on to the FTO, the substrates were shifted into the muffle furnace for annealing at 500°C for 1 hr.

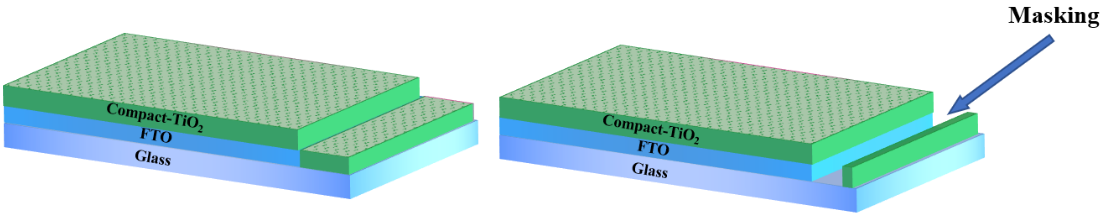

Figure 2: Schematic structure when the c-TiO2 layer was deposited on to the FTO substrate and masking of substrate

2.9 Preparation of mesoporous TiO_2 (mp-TiO_2) layer by spin-casting.

After fabrication of c-TiO_2 layer, the substrate was cooled down at room temperature After that substrates were transferred on the spin-coater to application of mp-TiO_2 film. The definite program was set in spin-coater machine for fabrication of the mp-TiO_2 layer. After fabrication mp-TiO_2 layer on to the substrate, the devices were shifted into the muffle furnace for drying at 500°C for 1 hr.

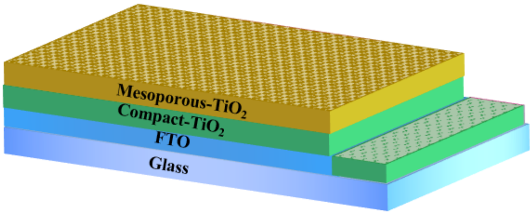

Figure 3: Schematic structure of the deposited mp-TiO_2 layer over c-TiO_2 layer

3.0 Preparation of ZnO sol-gel layer by spin-casting

The ZnO sol-gel was produced by countering of zinc acetate dihydrate and 2-methoxyethanol for 12 hrs at room temperature. On top of the c-TiO_2 / mp-TiO_2 layer, the ZnO layer was spin-coated by using ZnO sol–gel solutions at 5000 rpm for 30 s. A cotton-swab dipped in acetone was used to remove the ZnO from the same area that was masked during-TiO_2 deposition to prevent the recombination and annealed the layer at 300°C for 1 hr.

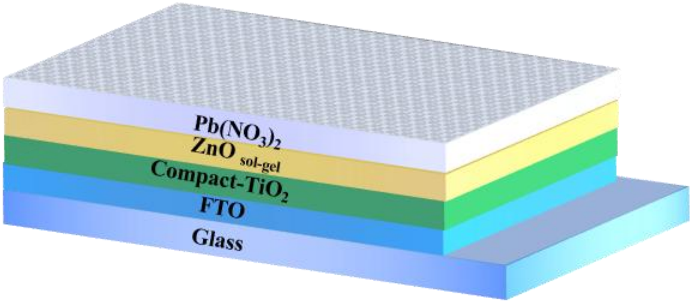

Figure 4: Schematic structure when the ZnOs-g layer was deposited on to the c-TiO_2/mp-TiO_2 layer

3.1 Preparation of $Pb(NO_3)_2$ layer by dip-coating method

To cope with PbI_2 conventional spin-casting process, we introduced novel $Pb(NO_3)_2$ film through simple dip-coating method to remove detrimental organic solvents (DMSO and DMF) which is obligatory for PbI_2. Furthermore, spin-casting method is not considerable for large surface area films for industrialization. In a general procedure, a c/mpTiO_2 layered beneath ZnO substrate were primarily dipped into 0.1M $Pb(NO_3)_2$ precursor solution dissolved into ethanol (EtOH)/water (2 : 1, v/v) for 30 sec. The substrate was rinsed using deionized water and then annealed at 120 C for 10 min, we obtained in a highly transparent layer over the substrate. The $Pb(NO_3)_2$ layer is l noticeably adsorb over zinc oxide surface.

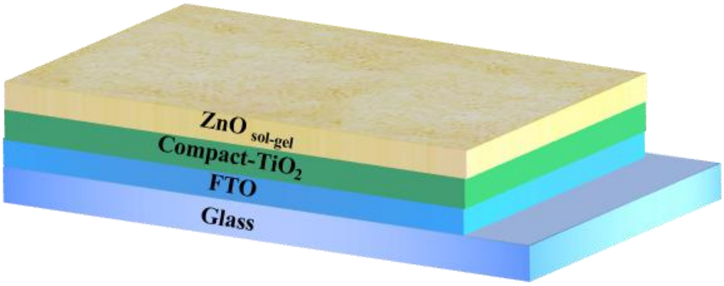

Figure 5: Schematic structure of the adsorbed $Pb(NO_3)_2$ layer over ZnO coated substrate

3.2 Preparation of Perovskite layer by dip-coating method

To fabricate $MAPbI_3$, $FAPbI_3$ and $MA_X FA_{1-x}PbI_3$ perovskite films via aqueous $Pb(NO_3)_2$, we utilized a sequential deposition coating (SDC) approach followed by numerous successive solid-state ion-exchange and reaction SSIER repetitions. The formamidine iodide (FAI) and Methylammonium iodide (MAI) solution was dissolved in isopropanol (IPA). The 0.63-M MAI and 0.58-M FAI solution was dissolved in isopropanol. The MAI/FAI mixed-halide perovskite layers were fabricated by using various concentrations of MAI/FAI of (0.7/0.3, 0.6/0.4, 0.5/0.5, 0.4/0.6, and 0.3/0.7), respectively in isopropanol for 30 s then dried at 120°C for 10 min under controlled humidity of less than 20%. This process developed single SSIER cycle. There were several SSIER repetitions occur to complete the reaction between Pb(NO3)2 and MAI/FAI

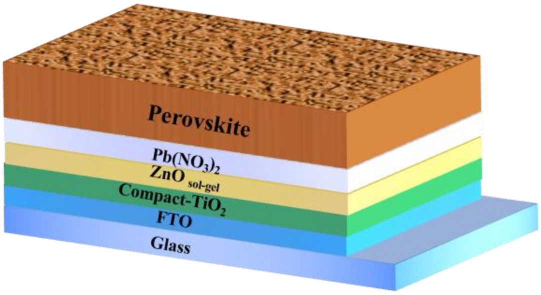

Figure 6: Schematic structure of the prepared $MAPbI_3$/ MA_X $FA_{1-x}PbI_3$ perovskite layers by a simple dip-coating technique

3.3 Spin-coating of spiro-OMeTAD layer

The spiro-OMeTAD was act as hole transport material and deposited through spin-coating at 3000 rpm for 30 sec. The HTM solution was obtained by dissolving 29 mg of spiro-OMeTAD, 7 mL of 170 mg mL- Li-TFSI in acetonitrile, and 11 mL of t-BPy to increase the performance of the devices. The perovskite and spiro-OMeTAD were clean through scalpel and wiped with cotton-swabbed rinsed with 2-methoxy ethanol. 2-methoxy ethanol was used for the reason that it take away the perovskite and spiro-OMeTAD without reacting to the FTO substrate. This was done on the similar area of the substrates that been free of compact and mesoporous TiO_2 with the reason to expose the FTO for the cathode contact.

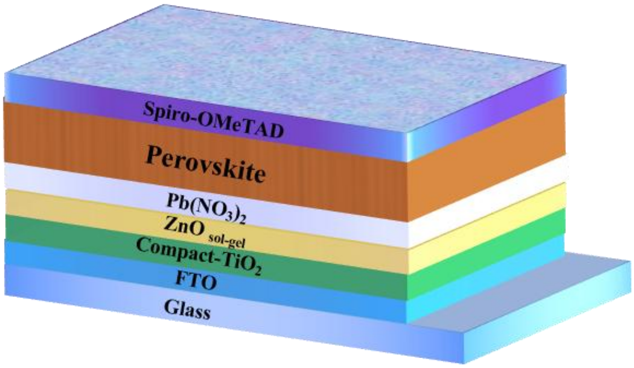

Figure 7: Schematic structure of the deposited spiro-OMeTAD layer over

$MAPbI_3$/ $MAPbI_{3-x}Cl_x$ perovskite layers

3.4 Thermal evaporation of MoO_3 and silver (Ag) Electrode

The prepared substrate were placed in a masked holder for deposition of metal on wanted surface area and then placed in the evaporator chamber. The evaporation initiated by lowering the pressure in the evaporator and once the pressure touched vacuum of $< 3.5\times10^{-6}$ mbar. Lastly, device fabrication was done by thermal evaporation of 10 nm thin MoO3 film and 100 nm Ag electrode over HTM film under compact pressure (less than 10^{-5} Torr).

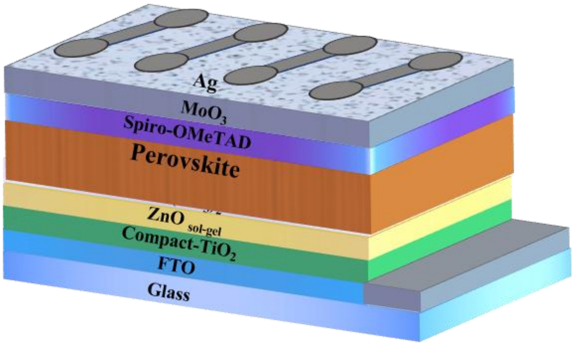

Figure 8: Schematic structure of the completely sequentially dip-coated processed perovskite layers fabricated perovskite solar cells device

Chapter 3

Controlling Phase and Morphology of All-Dip-Coating Processed HC(NH2)2PbI3 Perovskite Materials from an Aqueous Halide-Free Lead Precursor

1. Introduction

Organic-inorganic lead halide perovskite have gained tremendous attention since they achieved remarkable performances via their excellent light-harvesting, long carrier diffusion lengths, and higher charge transport behaviors [1]. These perovskite materials were usually composed of inorganic lead cores bridged with organic species of cationic alkylammonium and anionic halide [2]. Among them, a methylammonium lead halide $MAPbX_3$ (X = Cl, Br, or I) perovskite material was mainly adapted as efficient direct-band-gap materials in the initial stage of PrSCs development and was readily prepared by the reaction of a lead halide (PbX_2) and methylammonium halide (CH_3NH_3X, MAX) [3]. Up to date, these perovskite materials have been extensively developed via various strategies to achieve high-efficiency perovskite solar cells (PrSCs) and accomplished an unprecedent power conversion efficiency (PCE) of ~25% [4]. Though, it's still challenging for scalable production and possible commercialization to develop more fascinate deposition technologies to overcome the substrate size limited by spin-casting deposition and the toxic use detrimental organic solvents (DMF and DMSO), that are being employed due to much poor/lower solubility of lead halide-based materials. Recently, we have developed an efficient deposition method of MAPbI3 materials by a simple and unique sequential dip-coating (SDC) process from a green halide-free lead precursor, Pb $(NO_3)_2$ for high efficiency PrSCs [5–8]. This SDC process facilitates the large area fabrication of an effective perovskite films with an aqueous halide-free lead precursor, which was being used because of their desirable affinity towards an environmentally friendly and cost-effective solvents such as water. However, the MA cation based $MAPbI_3$ perovskite films has been described to be unstable in contrast to heat and light because of its lower crystallization energy and reversible phase transition from tetragonal to cubic even at rather a lower temperature of ~55 ◦C [2]. Thus, it has been expressive to explore the cationic species for more efficient organic-inorganic lead halide perovskite materials with smaller bandgap as well as superior photo and thermal stability to replace MA cation (MA^+) [3]. The incorporating of formamidinium cation ($CH(NH_2)^{2+,}$ FA^+) species, which possesses large ionic radius [4], perovskite crystal lattice has been recently proposed as potential alternatives because of its longer charge carrier diffusion lengths, and higher phase transition temperature compared to those with MA^+ group [9,10]. Regarding this, we have also interested in FAPbI3 perovskite layers deposited by all-dip-coating process from an aqueous halide-free lead precursor. The FAPbI3 perovskite layers were often prepared via solution-processed deposition followed by thermally annealing approach which is required to convert into a crystalline form of as prepared $FAPbI_3$, in which two polymorphs states were usually observed; a blackish α-$FAPbI_3$ phase is a cubic perovskite structure with a direct band-gap of ~1.47 eV and a yellowish δ-APbI3 phase is a hexagonal non-perovskite structure with an in-direct band-gap of ~2.48 eV [11–13]. The optically active α-$FAPbI_3$ structure is observed as stable phase even at high temperature over 150 ◦C while the photo-inactive δ-$FAPbI_3$ structure is mainly found at ambient and humid environment owing to the lowest free energy of formation [14]. Because these two phases frequently coexisted in $FAPbI_3$ layer, the application of $FAPbI_3$ perovskite material for high-efficiency PrSCs has still suffered from phase purity issues [15, 16]. Thus, several approaches such as additive assisted one-step methods or improved two-step methods have been attempted to the α-$FAPbI_3$ dominant crystallization by kinetical control [16–19]. Also, the thermal annealing step of as-prepared FAPbI3 layers should be a crucial process to achieve better photovoltaic performance in PSCs device because δ-$FAPbI_3$ phase could be converted directly into α-FAPbI3 phase by thermal treatment in which the volume of the unit cell can be expanded [16, 20–22, 27]. Considered to these, in this study, we have attempted the all-dip-coating deposition of $FAPbI_3$ perovskite layers from an aqueous halide-free lead precursor as a unique, easy, cost-effective, and environmentally friendly process. And we have tried to modulate the phase and morphology of all-dip-coating processed $FAPbI_3$ material to use efficiently in PrSC devices. Interestingly, we found that the phase and morphology of $FAPbI_3$ material fabricated using this process can be significantly influenced by the concentration of FAI dipping solution of as-prepared $Pb(NO_3)_2$ layer as well as annealing temperature of as-prepared $FAPbI_3$ layer during all-dip-coating deposition process from an aqueous halide-free lead precursor. Herein, we successfully demonstrated the all-dip-coating deposition of an efficient $FAPbI_3$ perovskite layers from an aqueous halide-free lead precursor and realized an efficient phase and morphology of $FAPbI_3$ crystalline layer by controlling the conditions adjusted simply during the all-dip-coating process from aqueous $Pb(NO_3)_2$ precursor over a thin ZnO/c-TiO_2 bilayer. The blackish α-$FAPbI_3$ perovskite layers were dominantly revealed at annealing temperature above 120 ◦C of as-prepared $FAPbI_3$ layers produced in an appropriate concentration of FAI solution. Although we tried to build only α-phase of $FAPbI_3$ layers from various methods during the all-dip-coating process, it has been still observed a little δ-$FAPbI_3$ and PbI_2 components in $FAPbI_3$ perovskite layers. Especially, we found the notable device performances and stability with a PCE of 10.83% in planar heterojunction (PHJ) PrSC devices with all-dip-coating proceed $FAPbI_3$ perovskite layer which was prepared at an annealing temperature of 120 ◦C of as-prepared $FAPbI_3$ layer fabricated by dipping of as-prepared $Pb(NO_3)_2$ layer in 0.06 M FAI solution. In Fig. 1 (a) schematic presentation of prepared $FAPbI_3$ perovskite material fabricated with all-dip-coating deposition, (b) n-i-p type PHJ PrSCs architecture, and (c) energy-level alignment of materials

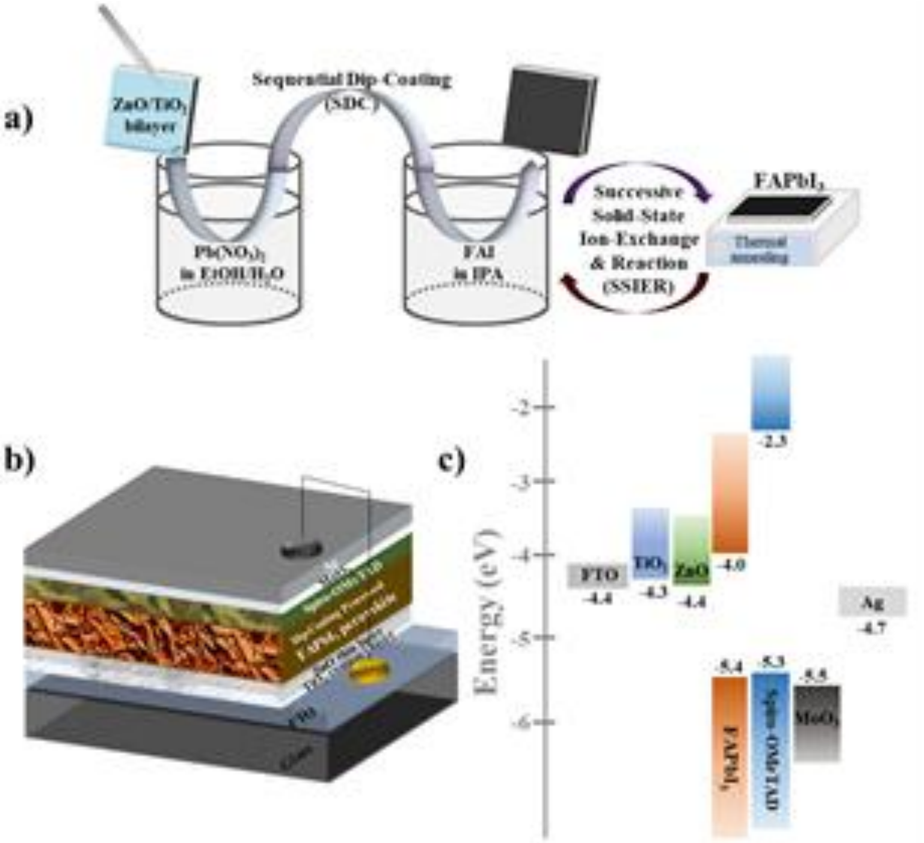

Figure 1 (a) Schematic description of prepared $FAPbI_3$ perovskite material fabricated with all-dip-coating deposition, (b) n-i-p type PHJ PrSCs architecture, and (c) energy-level diagram of studied materials.

Results and Discussion

In a simple all-dip-coating process to deposit FAPbI3 thin layer of perovskite by, a halide-free Pb precursor layer was firstly prepared by dipping the thin ZnO/c-TiO2 bilayer electron transport layer (ETL) in an aqueous $Pb(NO_3)_2$ solution as shown in Figure 1a. The $Pb(NO_3)_2$ layer is likely to adsorb rapidly over ZnO layer and then readily transformed into darkish brown-coloured thin films when immersed into the FAI solution, ensuring the formation of FAPbI3 perovskite materials that processed very rapidly even in a very short period of the 30s. However, these FAPbI3 films are immediately decomposed into a yellowish PbI2 crystalline morphology while solvent evaporation at 120℃ even at lower relative humidity (less than 20%). Thus, we tried to prepare the stable $FAPbI_3$ films by applying the successive solid-state ion-exchange and reaction (SSIER) cycles.5-8 In this study, we investigated the performances and characteristics of the efficient and stable $FAPbI_3$ materials fabricated through the simple all-dip-coating and the successful SSIER processes. All the fabrication experiments were carried-out in an ambient air environment (less than 20% relative humidity) unless stated otherwise. Interestingly, we found that the crystallinity and morphology of the deposited FAPbI3 layers were significantly affected by the concentration of FAI solution, not dipping duration time. We here varied the concentration of FAI solution with 0.05 M, 0.06 M, and 0.07 M. Figure 2 shows (a-d) the SEM surface morphologies and (e) XRD patterns of $FAPbI_3$ films deposited by the all-dip-coating process with three FAI solutions (0.05-FAI (green line), 0.06-FAI (red line), and 0.07-FAI (black line) and (f)the correlated FAPbI3 conversion factors and α-FAPbI3 phase growth ratios. The as-prepared $FAPbI_3$ films fabricated by dipping $Pb(NO_3)_2$ layers into these designated FAI solutions were dried at 120℃ for 10 min. As shown in Figure 2a-d, the $Pb(NO_3)_2$ layer exhibited a particulate morphology with good surface coverage over ZnO/c-TiO2/FTO glass substrate. And the formed dip-coating processed $FAPbI_3$ films grown from these particulate $Pb(NO_3)_2$ presented structural morphologies having submicron-sized crystal lumps with indistinct grain boundaries (pin-holes) and good surface morphologies and coverages. These morphologies might enable efficient charge transport and suppress interfacial recombination between the ETM and HTM layers, expecting the good performances of PHJ PrSC devices.

Particularly, we found that the microstructural evolution of $Pb(NO_3)_2$ layers into $FAPbI_3$ materials revealed obvious dependency on the concentration of FAI solution. Although all the $FAPbI_3$ films deposited by the all-dip-coating approach presented similar surface morphologies with a uniform grain size distribution, the higher concentration of FAI solution induced the more proportion of rod-like $FAPbI_3$ material which was known well as hexagonal δ-phase structures [13-23]. These note that the concentration of FAI solution can significantly affect to the crystal growth preferred kinetically between cubic α-phase and hexagonal δ-phase when the $FAPbI_3$ structures are conducted via reaction of $Pb(NO_3)_2$ and FAI. As shown in Figure 2e, the $FAPbI_3$ films deposited by the all-dip-coating process with 0.05-FAI (green line), 0.06-FAI (red line), and 0.07-FAI (black line) presented typical XRD patterns of cubic α-$FAPbI_3$ crystallinities at $2\theta = 13.8°$ corresponds to (001) diffraction planes.16,24-25 The corresponding peaks to PbI_2 and δ-$FAPbI_3$ (100) at $2\theta = 11.8°$ and 12.7°, respectively were partially detected in these $FAPbI_3$ films.11,13-14 The enlarged XRD patterns in the 2θ range from 10° to 15° are also illustrated in Figure S1 of supporting information. Based on these XRD patterns, we also determined the α-$FAPbI_3$ phase growth ratios (Gα-$FAPbI_3$) from the specific peak intensities of α-$FAPbI_3$ and δ-$FAPbI_3$ at $2\theta = 13.8°$ and 11.8°,

$$G\alpha\text{-FAPbI3} = I13.8°/(I11.8° + I13.8°) \qquad (1)$$

Also, the conversion factors of $FAPbI_3$ ($CFAPbI_3$) could be qualitatively defined using the peak intensities of PbI_2, δ-$FAPbI_3$, and α-$FAPbI_3$ at $2\theta =$ 12.7°, 11.8°, and 13.8°, respectively.5-7

$$CFAPbI_3 = (I11.8° + I13.8°)/(I12.7° + I11.8° + I13.8°) \qquad (2)$$

As shown in Figure 2f, the Gα-$FAPbI_3$ and $CFAPbI_3$ values could be significantly depends on the concentrations of FAI solution. The $FAPbI_3$ material prepared with 0.07-FAI exhibited the highest conversion value for $FAPbI_3$ generated from PbI2 than those of 0.05-FAI and 0.06-FAI. This indicates that the higher FAI concentration gave a higher conversion into FAPbI3 by increasing the reaction chance of a lead precursor in FAI solution. Meanwhile, the $FAPbI_3$ material prepared with 0.05-FAI presented the most α-$FAPbI_3$ phase growth in $FAPbI_3$ generated from PbI_2 than those of 0.06-FAI and 0.07-FAI. A high concentration of FAI might interrupt the α-$FAPbI_3$ phase perovskite formation due to the kinetically preferred crystal growth into δ-$FAPbI_3$ phase by the low free energy of formation at ambient environment.11, [13, 16]. These results are well interrelated with the surface morphologies (Figure 2b-d). Considered to these results observed in Figure 2, we proceeded a further study with the most effective FAPbI3 perovskite layer fabricated with 0.06-FAI, which exhibited efficient surface morphologies and crystallinities to lead the better performances in PrSC

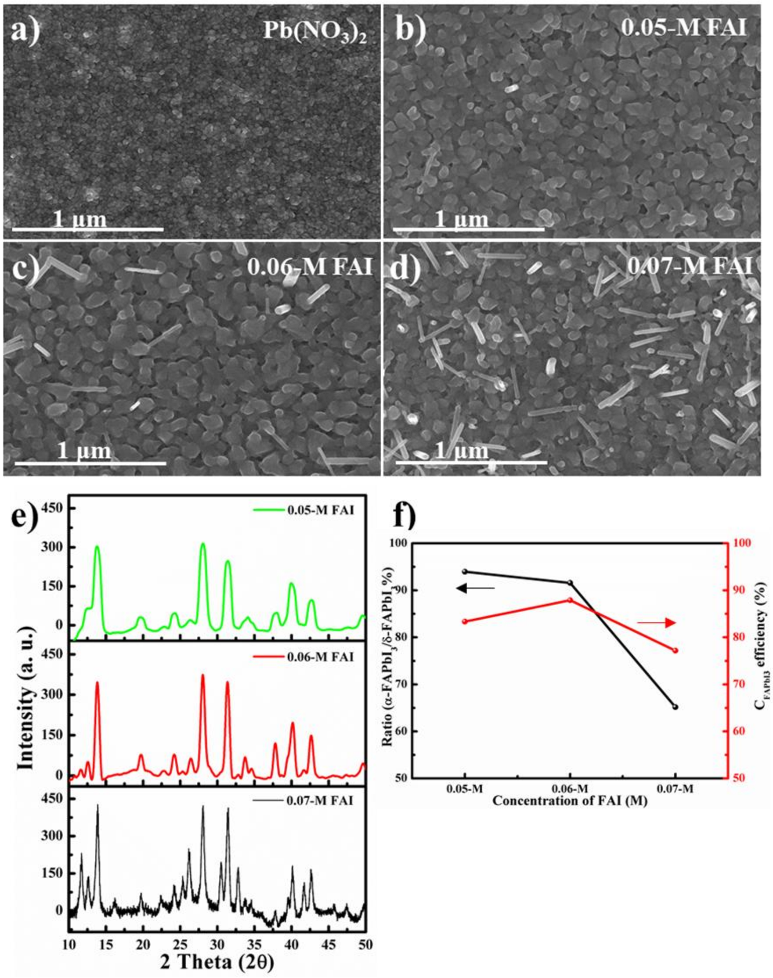

Figure 2. (a-d) FESEM surface morphologies and (e) XRD patterns of $FAPbI_3$ films deposited by the all-dip-coating process with three FAI solutions (0.05-FAI (green line), 0.06-FAI (red line), and 0.07-FAI (black line) and (f) the correlated $FAPbI_3$ conversion factors and α-$FAPbI_3$ phase growth ratios.

Considered to these results observed in Figure 2, we proceeded a further study with the most effective $FAPbI_3$ perovskite layer fabricated with 0.06-FAI, which exhibited efficient surface morphologies and crystallinities to lead the better performances in PrSC devices. Figure 3 displays the (a) UV-vis absorption and (b) PL spectra of $FAPbI_3$ layers deposited on the top of ZnO layer by all-dip-coating process with these FAI solutions (0.05-FAI (green line), 0.06-FAI (red line), and 0.07-FAI (black line) by thermal treatment at 120℃ for 10 minutes. All perovskite films were fabricated in the atmosphere under the controlled humidity below 20% because the blackish α-$FAPbI_3$ phase can change into the undesirable yellowish δ-$FAPbI_3$ phase under humid environment. We found that the optical properties of these $FAPbI_3$ films were remarkably affected by the adapted FAI concentrations. These exhibited the typical absorption behaviours of $FAPbI_3$ perovskite films with onset points of ~825 nm (optical band gap < 1.5 eV)13 with a slightly turbid appearance. Interestingly, it was observed that the higher FAI concentration led to attractive light absorption efficiency at a wavelength range of below 550 nm by fixing their baselines to a ~850 nm, representing the increments of yellowish δ-$FAPbI_3$ phase contained in $FAPbI_3$ perovskite films in higher FAI concentrations.16 This could well correspond with the results shown in Figure 2. Meanwhile, the $FAPbI_3$ perovskite film fabricated with 0.06-FAI presented the lowest PL intensity value of an intense peak observed around 796 nm compared to those with 0.05-FAI and 0.07-FAI as shown in Figure 3b.13-16 This shows that $FAPbI_3$ perovskite layers prepared with 0.06-FAI displays improved charge transformation behavior into the ZnO/c-TiO_2 bilayer ETL in-contrast with 0.05-FAI and 0.07-FAI. From these results, we could expect that the composition of photo-inactive components such as PbI2 and δ-$FAPbI_3$ in $FAPbI_3$ perovskite layer might affect significantly to photovoltaic performances in PrSC devices.

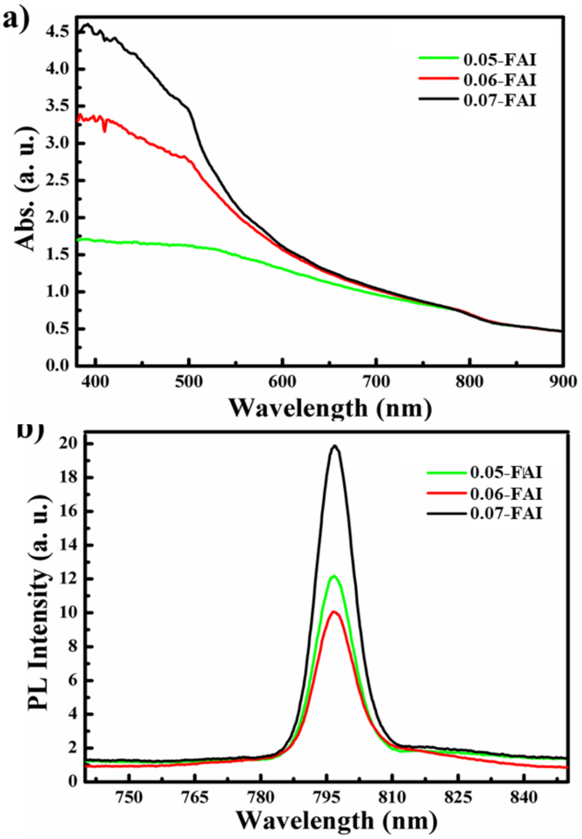

Figure 3 displays the (a) UV-vis absorption and (b) photoluminescence (PL) spectra of $FAPbI_3$ layers deposited on the ZnO/c-TiO_2 ETL layer by completely dip-coating process with these FAI solutions (0.05-FAI (green line), 0.06-FAI (red line), and 0.07-FAI (black line) annealed at 120℃ for 10 minutes

Next, we investigated the annealing temperature efficacy for all-dip-coating processed $FAPbI_3$ perovskite films because the thermal annealing step could induce the direct conversion into the α-$FAPbI_3$ phase of δ-$FAPbI_3$ phase by thermal treatment. The as-prepared $FAPbI_3$ films fabricated by dipping $Pb(NO_3)_2$ layers into 0.06M FAI solutions were dried at the designated temperatures in the air under controlled humidity of ~20% for 10 min. In this work, we varied the annealing condition with four temperatures of 80, 100, 120, and 150℃.

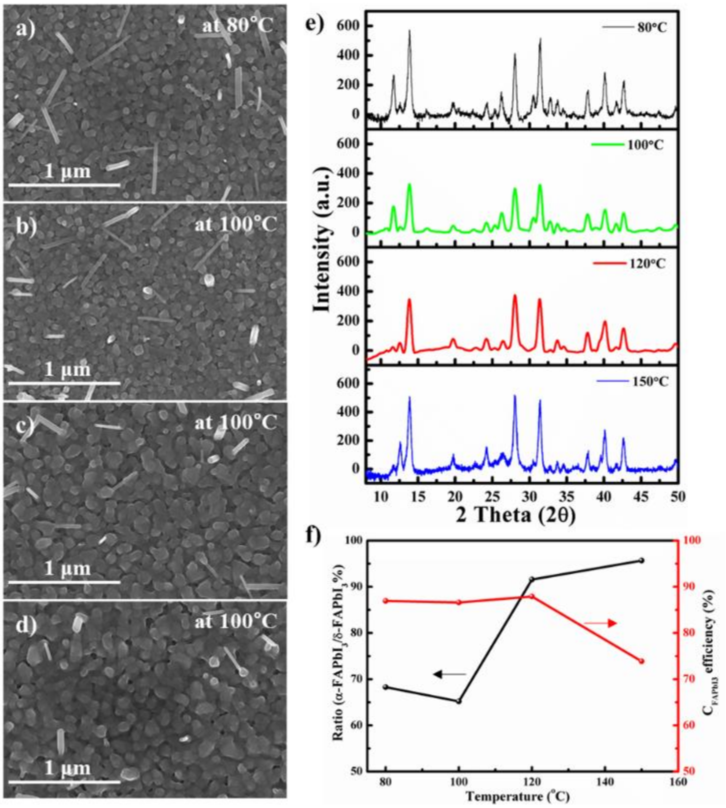

Figure 4. (a-d) FESEM surface morphologies and (e) XRD patterns of $FAPbI_3$ films deposited by the all-dip-coating process with four annealing temperature of 80 (black line), 100 (green line), 120 (red line), and 150℃ (blue line) and

(f) the correlated $FAPbI_3$ conversion factors and α-FAPbI3 phase growth ratios.

the Figure 4 shows (a-d) the SEM surface topologies and (e) XRD patterns of $FAPbI_3$ films deposited by the all-dip-coating process with four annealing temperature of 80 (black line), 100 (green line), 120 (red line), and 150℃ (blue line) and (f) the correlated $FAPbI_3$ conversion factors and α-$FAPbI_3$ phase growth ratios. As shown in Figure 4a-d, all $FAPbI_3$ layers exhibited good surface coverage over ZnO/c-TiO_2/FTO substrate, but it was interestingly found that the distinct grain boundaries in surface morphologies of $FAPbI_3$ materials were gradually disappeared following increasing of annealing temperature. Moreover, the higher annealing temperature of FAI solution induced the less proportion of rod-like hexagonal δ-$FAPbI_3$ phase structures, indicating the direct conversion into α-$FAPbI_3$ phase from δ-$FAPbI_3$ phase during annealing at high temperatures. These note that the annealing temperature of as-prepared $FAPbI_3$ layer can significantly affect the crystal growth preferred thermodynamically between cubic α-phase and hexagonal δ-phase. Also, as shown in Figure 4e and Figure S2, the XRD patterns of these FAPbI3 films presented the significantly reduced peak intensities of δ-$FAPbI_3$ phase in accordance with increasing of annealing temperature, correlating well with the reduced proportion of rod-like hexagonal δ-$FAPbI_3$ phase structures on their SEM surface morphologies in Figure 3a-d. Particularly, their Gα-$FAPbI_3$ and C$FAPbI_3$ values also revealed with substantial dependency on the annealing temperature of as-prepared $FAPbI_3$ layer (Figure 4f) The $FAPbI_3$ layer annealed at 120℃ and 150℃ gave high Gα-$FAPbI_3$ values of 92.% and 95%, respectively, but the $FAPbI_3$ layer annealed at 80°C and 100°C gave rather low Gα-FAPbI3 values of 68% and

65%, respectively. This indicates that the higher annealing temperature induced the more α-$FAPbI_3$ phase growth in $FAPbI_3$. While the $FAPbI_3$ layers annealed at 80, 100, and 120℃ exhibited high $CFAPbI_3$ values of 86, 86, and 87%, respectively, the thermal annealing of $FAPbI_3$ layer at 150℃ dramatically decreased its CFAPbI3 value (73%), indicating the decomposition of $FAPbI_3$ structure under high temperature.

Afterward, we investigated the devices performances of the fabricated PrSC devices with the $FAPbI_3$ layers through a simple SDC process in FAI solutions and an aqueous $Pb(NO_3)_2$ solution and determined their optimum performances by evaluating more than 200 fabricated PrSC devices. These PHJ PrSC devices were prepared with n-i-p type configuration of FTO/c-TiO_2/ZnO/$FAPbI_3$/spiro-OMeTAD/MoO_3/Ag [5-7]. The doping agents such as t-Bpy and Li-TFSI were doped in spiro-OMeTAD to improve the conductivity and efficiency of HTM. Figure 5 displays the current-voltage (J–V) curves for the highly efficient PrSCs constructed on $FAPbI_3$ perovskite films prepared (a) with three FAI solutions (0.05-FAI (green dotted line), 0.06-FAI (red dotted line), and 0.07-FAI (black dotted line)), which were thermally annealed at 120℃ and (b) with four annealing temperatures (80 (black dotted line), 100 (green dotted line), 120 (red dotted line), and 150℃ (blue dotted line), which were prepared with 0.06-FAI. The outcomes achieved while the optimization of the devices has also been summarized in Table S1 and S2. As shown in Figure 5, an efficient device achievement is seen with the $FAPbI_3$ perovskite films fabricated using 0.06-FAI and annealing temperature at 120℃; the PCEs with a maximum/average of 10.83%/10.72% with a short-circuit current density (Jsc) of 19.09 mA·cm-2, open-circuit voltage (Voc) of 0.93 V, and fill factor (F.F) of 0.61. The distribution of this device performance is illustrated in Figure S3. In Figure 5a, the devices prepared with all-dip-coating processed FAPbI3 perovskite layers prepared with 0.06-FAI displayed superior performance than 0.05-FAI and 0.07-FAI carried out under the same conditions; the PCEs of 8.55%/8.46% (with Jsc = 15.58 mA·cm-2, Voc = 0.98 V, and F.F = 0.56) and 7.91%/7.50% (with Jsc = 14.24 mA·cm-2, Voc = 1.01 V, and F.F = 0.55), respectively. And as shown in Figure 5b, the PrSC devices with all-dip-coating processed $FAPbI_3$ perovskite layers fabrication using annealing temperature of 120℃ presented a distinguished performance compared to those using annealing temperature of 80, 100, and 150℃ carried out under the same conditions; the PCEs of 7.20%/6.97% (with Jsc = 15.60 mA·cm-2, Voc = 0.84 V, and F.F = 0.55), 8.65%/8.39% (with Jsc = 20.47 mA·cm-2, Voc = 0.88 V, and F.F = 0.48), and 9.18%/8.79% (with Jsc = 17.44 mA·cm-2, Voc = 0.94 V, and F.F = 0.56), respectively. The higher Jsc values in these devices with $FAPbI_3$ perovskite films fabricated with 0.06-FAI and annealing temperature at 120℃ gave the better PCEs compared to those fabricated with other conditions. These results may have been caused by the superior $G\alpha$-$FAPbI_3$ and $CFAPbI_3$ factors, which are related α-phase crystallinity and productivity, respectively, of $FAPbI_3$ material generated through PbI_2 intermediate from $Pb(NO_3)_2$ precursor because the photo-inactive components such as PbI_2 and δ-$FAPbI_3$ in $FAPbI_3$ perovskite layer might interrupt efficient charge transports [10,13]. Even though the $FAPbI_3$ based PrSC devices prepared by a simple SDC approach exhibited the rather low PCE values compared those of $FAPbI_3$ based PrSC devices reported previously [2,13], these results might provide that this work can add more significance to the development of more fascinate deposition technology to overcome the well-established spin-casting deposition limiting substrate size and the usage of toxic and detrimental organic solvents.

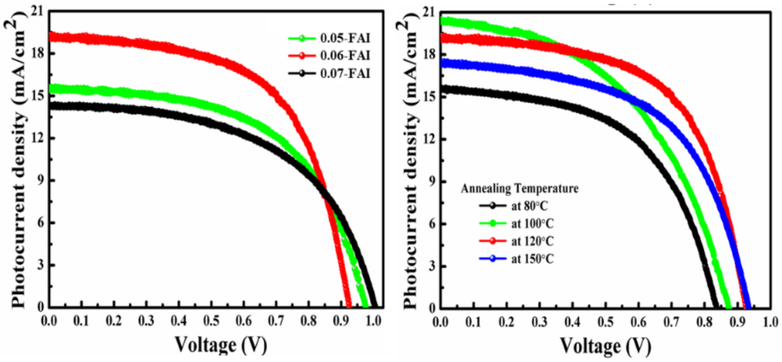

Figure 5. The J–V curves using AM 1.5 irradiation (100 mW·cm-1) for the most efficient PrSCs based on FAPbI3 perovskite layers fabricated (a) with three FAI solutions (0.05-FAI (green dotted line), 0.06-FAI (red dotted line), and 0.07-FAI (black dotted line)), which were thermally annealed at 120℃ and (b) with four annealing temperatures (80 (black dotted line), 100 (green dotted line), 120 (red dotted line), and 150℃ (blue dotted line)), which were prepared with 0.06-FAI.

On the other hand, the J-V hysteresis phenomenon for both scan directions (reverse or forward) has been often presented with n-i-p type PrSC devices with the TiO_2 electrode owing to differential charge extraction (or transportation) rates of holes and electrons which are separated from excitons [5-7]. Figure 6 displays (a) the hysteric behaviour of J-V curves and (b) operational stability, which was conducted under N_2 environment and without any encapsulation using AM 1.5 1 sun irradiation continuously, using the champion $FAPbI_3$ device fabricated by a simple SDC approach using 0.06-FAI and annealing temperature at 120℃. The corresponding values can be seen in Table S2. Interestingly, it was realized that majority of PrSCs devices presented insignificant differences with a little deviation in Jsc and Voc values in both directions, except the F.F values that is slightly lowered during forward scan. This might be caused by interfacial recombination dominated by impurity issue of PbI= and δ-$FAPbI_3$ in $FAPbI_3$ perovskite layer. The PrSC devices with $FAPbI_3$ perovskite layer prepared by a simple SDC approach also showed good EQEs under light absorption area, where the integrated photo-current values are in fine correlation with the Jsc values, (Figure S4) and an attractive operational stability of devices is seen without any substantial lowering of photovoltaic device performances for up to 400 hrs.

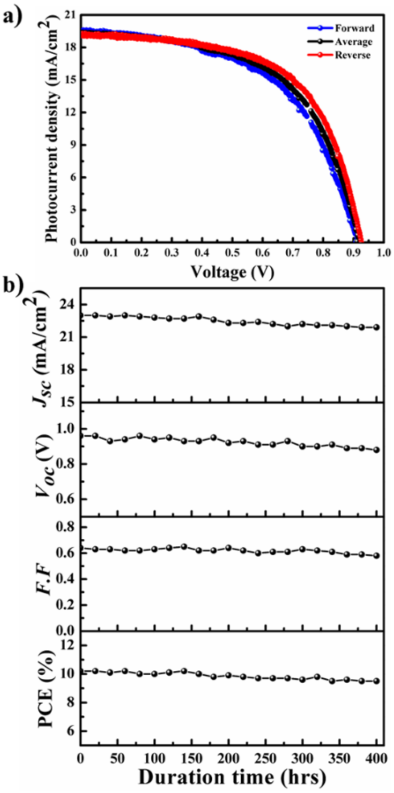

Figure 6. (a) The hysteric behaviour of the J-V curves measured for forward and reverse scan directions and (b) operational stability for the best-

performing PrSC devices from completely dip-coating processed $FAPbI_3$ perovskite layers.

Conclusion

We have presented the preparation of an efficient $FAPbI_3$ perovskite layers deposited by a simple and unique all-dip-coating deposition process using an aqueous non-halide lead precursor towards a facile, low-cost, non-toxic and environmentally friendly manufacturing approach for highly-efficient PrSCs. In this study, we realized the efficient phase and morphology of $FAPbI_3$ crystalline layers by controlling several conditions such as FAI concentration and annealing temperature adjusted in the all-dip-coating approach from aqueous $Pb(NO_3)_2$ precursor. Moreover, we could propose a new evaluating method on to develop an efficient FAPbI3 perovskite layer for high-efficiency PrSCs by determining the $G\alpha$-$FAPbI_3$ and $CFAPbI_3$ values as α-$FAPbI_3$ phase growth factor and $FAPbI_3$ formation factor, respectively, of $FAPbI_3$ perovskite layer. The most efficient $FAPbI_3$ perovskite layers were observed at annealing temperature above 120℃ of as-prepared $FAPbI_3$ layers produced in 0.06 M FAI solution. Although the blackish α-$FAPbI_3$ phase was dominantly revealed at high annealing temperatures above 120℃ and FAI concentration. it has been still observed a little δ-FAPbI3 and PbI2 components in $FAPbI_3$ perovskite layers. We found the composition factor of photo-inactive components such as PbI_2 and δ-$FAPbI_3$ in $FAPbI_3$ perovskite layer affected significantly to photovoltaic performances in PrSC devices. Nonetheless, the notable device performances and stability with a PCE of 10.83% in PrSC devices with all-dip-coating proceed $FAPbI_3$ perovskite layer under the optimized condition. Even though the PCEs obtained in PrSC devices with the all-dip-coating proceed $FAPbI_3$ perovskite layers were rather low values compared those of $FAPbI_3$ based PrSC devices reported previously, we believe these results might add more significance to the development of more fascinate deposition technology to overcome the well-established spin-casting approach limiting substrate size and the usage of toxic and detrimental organic solvents for high-efficiency PrSCs..

Chapter 4

Simple Preparation of Highly Efficient $MA_xFA_{1-x}PbI_3$ Perovskite films form an Aqueous Halide-Free Lead Precursor by All Dip-Coating Approach and Application in High Performance Perovskite Solar Cells

Introduction

Perovskite solar cells (PrSCs) based on organic-inorganic halide perovskites have been extensively studied in recent years because of their high PCEs, ease in fabrication and low preparation cost.[1-2]The excellent performances of PrSCs devices take advantage of perovskite materials contained inorganic lead bridged cores with organic cationic species (alkylammonium) and anionic halide. Amongst, the direct band-gap material such as methylammonium lead halide $MAPbX_3$ (X= I, Br or Cl) was employed at the preliminary phase of PrSCs by reacting with lead halide (PbX_2) and methylammonium halides (CH_3NH_3X, MAX). These perovskite materials are superior because of their broader light absorption range, lower exciton binding energy, adequate optical band-gap and higher charge transportation.[3] Although the $MAPbI_3$ perovskite material, having a direct bandgap of 1.57 eV, has been specifically employed as the light harvesters in PSCs, it was reported that $MAPbI_3$ perovskite films undergo degradation in light and heat mainly in the existence of solvents or humidity and possess inadequate short-circuit photocurrent density (J_{sc}).[4,6] Moreover, when the temperature exceeds beyond 60℃, the $MAPbI_3$ perovskite films faced phase transition behavior because of its lower crystallization energy. Recently, $FAPbI_3$ perovskite material incorporated formamidinium cation $[HC(NH_2)^{2+}$, FA) has been considered as high performing perovskite materials because it possesses a higher photo and thermal stability and lower bandgap (1.34 eV) to replace $MAPbI_3$ PrSCs.[7-8] The $FAPbI_3$ perovskite layers often prepared with the solution deposition process and required specific heating process to transform the deposited solution into a crystalline form. However, $FAPbI_3$ perovskite films show inherent instability and found into two polymorphs states; a perovskite blackish phase (α-FAPbI$_3$) and a non-perovskite yellowish phase (δ-FAPbI$_3$). At ambient temperature, the black α-FAPbI$_3$ phase which is employed as a specific light-absorbing layer in PSCs devices[9] is so non-stable that it transforms into the perovskite-free yellow δ-FAPbI$_3$ phase readily.[10]By considering these, it seems that the MAPbI$_3$ and FAPbI$_3$ has specific drawbacks as absorption materials of PrSCs when used independently. Therefore, many research groups have explored extensively the usage of mixed organic-cation perovskite layers such as $MA_xFA_{1-x}PbI_3$ to overcome the disadvantages of PSCs devices with single cation perovskite films.[11-13] Mixed organic cation ($MA_xFA_{1-x}PbI_3$) perovskite layers have exhibited various advantages to further enhance the PCE and stability of PSCs films because MA cation stabilizes the α-FAPbI$_3$ perovskite films and stops their conversion into δ-FAPbI$_3$ perovskites at room temperature.[14] Also, researchers have reported some extra-ordinary features of mixed organic-cationic perovskite films as an efficient light absorber: a high defect tolerance, a suitable tunable bandgap, a longer charge carrier diffusion lengths, higher absorption co-efficient and a bi-polar charge transport characteristics. These parameters are the key factors in improving the photovoltaic performance of PrSCs devices.[1-4]

Up to date, PrSCs have attained great success via various strategies and the efficiency of PSCs devices boosted up to 25.2%, analogous to those of polycrystalline solar cells.[3] But still, it is challenging enough for industrial applications by advancing the advanced deposition technologies to minimize the threat of the size limitations caused by conventional spin-coating process as well as usage of detrimental organic solvents (DMSO and DMF), used to dissolve lead halide precursors. Very recently, we have reported an effective strategy to deposit methylammonium (MA) lead halide ($MAPbI_3$) perovskite materials by an advanced, simple, and unique all sequential-dip-coating (SDC) method from an aqueous halide-free lead precursor, $Pb(NO_3)_2$ for efficient PrSCs. The SDC approach proves better to efficiently dominate the size limitations caused by conventional spin-coating process and can produce larger-area device fabrication of an efficient perovskite films prepared with an aqueous $Pb(NO_3)_2$, which was being used because of its affinity with non-toxic, low cost and environmental solvents, like water. Because of these, in the present study, we have also make an effort to employ the all sequential-dip-coating approach to prepare $MA_xFA_{1-x}PbI_3$ perovskites from an aqueous halide-free $Pb(NO_3)_2$ as a simple, low-cost and an environmentally benign method. We have also modulated the phase and surface crystallinity of $MA_xFA_{1-x}PbI_3$ perovskites from all sequential-dip-coating approach to fabricate an efficient PSCs device.

Herein, we effectively established all-sequential-dip-coating approach of an efficient $MA_xFA_{1-x}PbI_3$ perovskite films prepared by a aqueous non-halide lead precursor solution. During sequential dip-coating of $Pb(NO_3)_2$ layer deposited over a ZnO covered c-TiO_2 bilayer substrate, efficient phase and surface morphologies of $MA_xFA_{1-x}PbI_3$ perovskite films were successfully realized by varying MAI/FAI molar ratios in precursor solution over as-prepared $Pb(NO_3)_2$ layer. The various grain sizes and boundaries as well as cubical lumps of $MA_xFA_{1-x}PbI_3$ perovskite crystal were also demonstrated after annealing at 120℃ of as-prepared $MA_xFA_{1-x}PbI_3$ perovskite layers obtained with appropriate concentrations of MAI and FAI solution. Interestingly, all-dip-coating processed $MA_xFA_{1-x}PbI_3$ perovskite films have no presence of δ-$FAPbI_3$ perovskites, even at low MAI insertion into the FAI solution. The fabricated PSCs devices ($MA_xFA_{1-x}PbI_3$) exhibited a superior performance with improved stabilities in planar heterojunction (PHJ) architecture with a notable PCE value of 14.1% all sequential-dip-coating deposition processed $MA_{0.5}FA_{0.5}PbI_3$ perovskite films prepared by incorporating as-deposited $Pb(NO_3)_2$ layer in MAI/FAI (1/1 molar ratio) solution.

Results and Discussion

Figure 1a shows the simple all sequential-dip-coating approach for the deposition of mixed cationic ligand based $MA_xFA_{1-x}PbI_3$ perovskite layers, an aqueous non-halide Pb precursor layer was initially deposited by dipping the ZnO covered c-TiO_2 bilayer electron transport layer (ETL) into the aqueous $Pb(NO_3)_2$ precursor solution.

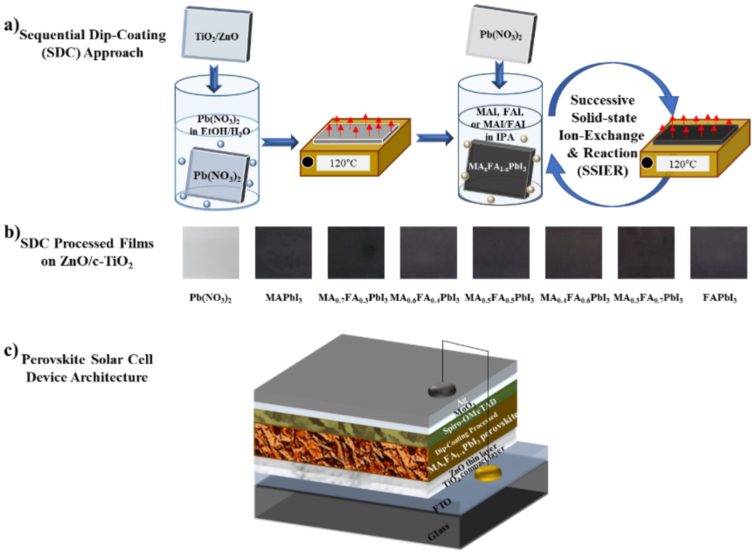

Figure 1. (a) Schematic route of $MA_xFA_{1-x}PbI_3$ perovskite layers prepared by sequential dip-coating approach, (b) their photographic images, and (c) the perovskite solar cell device architecture adapted in this study.

The $Pb(NO_3)_2$ layer from an aqueous solution rapidly adsorb over ZnO surface and then likely to transform into dark-brown and a blackish-colored film when exposure into pure MAI, FAI or MAI/FAI mixed-precursor solution, confirming the formation of $MAPbI_3$, $FAPbI_3$, or $MA_xFA_{1-x}PbI_3$ perovskite films, respectively, although for a quite short span of time of the 30s. Nevertheless, since these perovskite layers instantly decomposed by leaving yellowish-colored PbI_2 crystallinity during heating at 120℃ (< 20% relative humidity),[20] we proceeded additional ion-exchange reactions by unreacted $Pb(NO_3)_2$ in these perovskite layers, which is defined as solid-state ion-exchange and reaction (SSIER), so that the more stable $MAPbI_3$, $FAPbI_3$, and $MA_xFA_{1-x}PbI_3$ perovskite films were achieved by applying successive repetition of SSIER cycles. In this study, the five-type $MA_xFA_{1-x}PbI_3$ ($MA_{0.7}FA_{0.3}PbI_3$, $MA_{0.6}FA_{0.4}PbI_3$, $MA_{0.5}FA_{0.5}PbI_3$, $MA_{0.4}FA_{0.6}PbI_3$, and $MA_{0.3}FA_{0.7}PbI_3$) perovskite layers prepared in different MAI/FAI molar ratios of 0.7/0.3, 0.6/0.4, 0.5/0.5, 0.4/0.6, and 0.3/0.7, respectively were characterized and compared to $MAPbI_3$ and $FAPbI_3$ perovskite layers prepared MAI and FAI solutions, respectively. Interestingly, these $MA_xFA_{1-x}PbI_3$ perovskite layers significantly affected by proportions of MAI/FAI and exhibited stable and much darker blackish-colored films compared to those of $MAPbI_3$ and $FAPbI_3$ as shown in Figure 1b, and were carried out on perovskite solar cell device for photovoltaic performances as shown in Figure 1c.

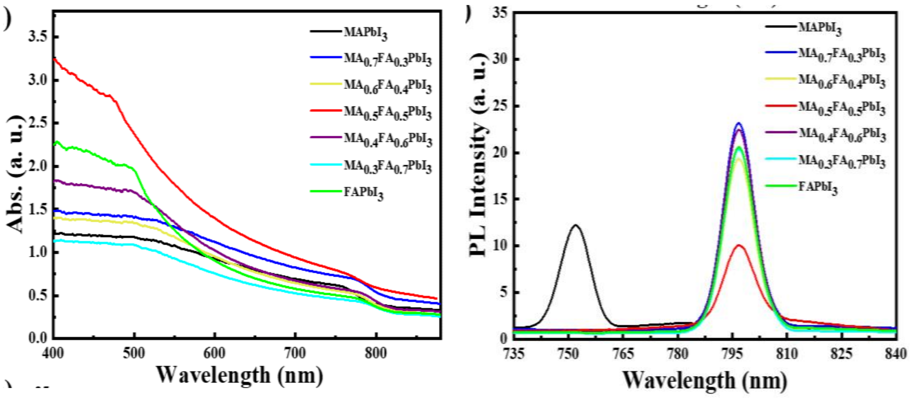

Figure 2. (a) UV-Vis absorption and (b) photoluminescence (PL) spectra for $MAPbI_3$, $FAPbI_3$ and MAI/FAI mixed-halide $MA_xFA_{1-x}PbI_3$ perovskite films prepared on ZnO/c-TiO_2/FTO substrate with MAI (black), FAI (green), and MAI/FAI mixed solutions with various molar ratios (0.7/0.3 (blue), 0.6/0.4 (yellow), 0.5/0.5 (red), 0.4/0.6 (purple), and 0.3/0.7 (cyan)) by all simple dip-coating approach.

Figure 2 shows the (a) UV-Vis absorption and (b) PL spectra for $MAPbI_3$, $FAPbI_3$ and MAI/FAI mixed-halide $MA_xFA_{1-x}PbI_3$ perovskite films prepared on ZnO/c-TiO_2/FTO substrate. All perovskite films which were prepared under controlled air humidity environment of not more than 20% and exhibited the distinctive absorption behavior of $MAPbI_3$ and $FAPbI_3$ perovskites with onset points of ~750 nm, ~825 nm, respectively[15,20] as shown in Figure 2a. The absorption edges wavelength for $FAPbI_3$ based perovskite materials were found to be longer than that of pure $MAPbI_3$ based perovskite materials. The related optical band-gap of $MAPbI_3$ and $FAPbI_3$ based perovskite materials were found to be comparable to the previously published reports of < 1.55 eV and < 1.48 eV, respectively.[22] Meanwhile, it was realized that $FAPbI_3$ films deposited in FAI precursor solution led to the higher light absorption efficiency at a wavelength range of below 550 nm when their baselines were adjusted to a ~850 nm, indicating the yellowish δ-$FAPbI_3$ phase.[20] Interestingly, we investigated that the optical characteristics of $MA_xFA_{1-x}PbI_3$ perovskites were meaningfully affected by modulating the MAI/FAI molar ratios. The lower band-gap of $FAPbI_3$ based perovskite materials indicate their lower symmetry than that of $MAPbI_3$ based perovskite, which can be adjusted by varying the FAI concentration into the MAI to form an efficient mixture solution to broaden the spectral response range. The higher FAI concentration in the FAI/MAI mixed halide solution led to turbid and dark blackish perovskite layers, thus, producing a non-uniform absorption behavior by light scattering in the UV-Vis absorption spectra. Among them, $MA_{0.5}FA_{0.5}PbI_3$ perovskite film fabricated in MAI/FAI (1/1 molar ratio) solution exhibited a much higher light-absorption efficiency compared to those of other concentration ratios, indicating superior surface crystallinity of perovskite films. Meanwhile, the $MAPbI_3$ and $FAPbI_3$ perovskite films exhibited typical PL intense peaks around 751 and 796 nm but the $MA_xFA_{1-x}PbI_3$ perovskite films presented PL intense peaks around 796 nm similar with that of $FAPbI_3$ not $MAPbI_3$.[3,23] From these results, we could expect that the characteristics of $MA_xFA_{1-x}PbI_3$ perovskite films fabricated in MAI/FAI mixture solution might be comparable to those of $FAPbI_3$. Interestingly, the $MA_{0.5}FA_{0.5}PbI_3$ Perovskite film exhibited the lowest PL intensity value than those of $FAPbI_3$ and $MAPbI_3$ as well as other subjected MAI/FAI solutions as shown in Figure 2b. This indicates that $MA_{0.5}FA_{0.5}PbI_3$ perovskite film shows better charge transfer behavior into the ZnO/c-TiO_2

ETL layer so that lead superior device performances in PrSC.

Regarding these results, we realized the surface morphologies of the aforementioned $MAPbI_3$, $FAPbI_3$ and $MA_xFA_{1-x}PbI_3$ perovskite films deposited on ZnO/c-TiO_2/FTO substrate. Figure 3 shows the FESEM surface morphologies of $MAPbI_3$, $FAPbI_3$ and $MA_xFA_{1-x}PbI_3$ perovskite films converted from (a) $Pb(NO_3)_2$ film adsorbed on ZnO/c-TiO_2/FTO substrate with (b) MAI, MAI/FAI mixed solutions with various molar ratios ((c) 0.7/0.3, (d) 0.6/0.4, (e) 0.5/0.5, (f) 0.4/0.6, and (g) 0.3/0.7), and (h) FAI by all simple dip-coating approach.

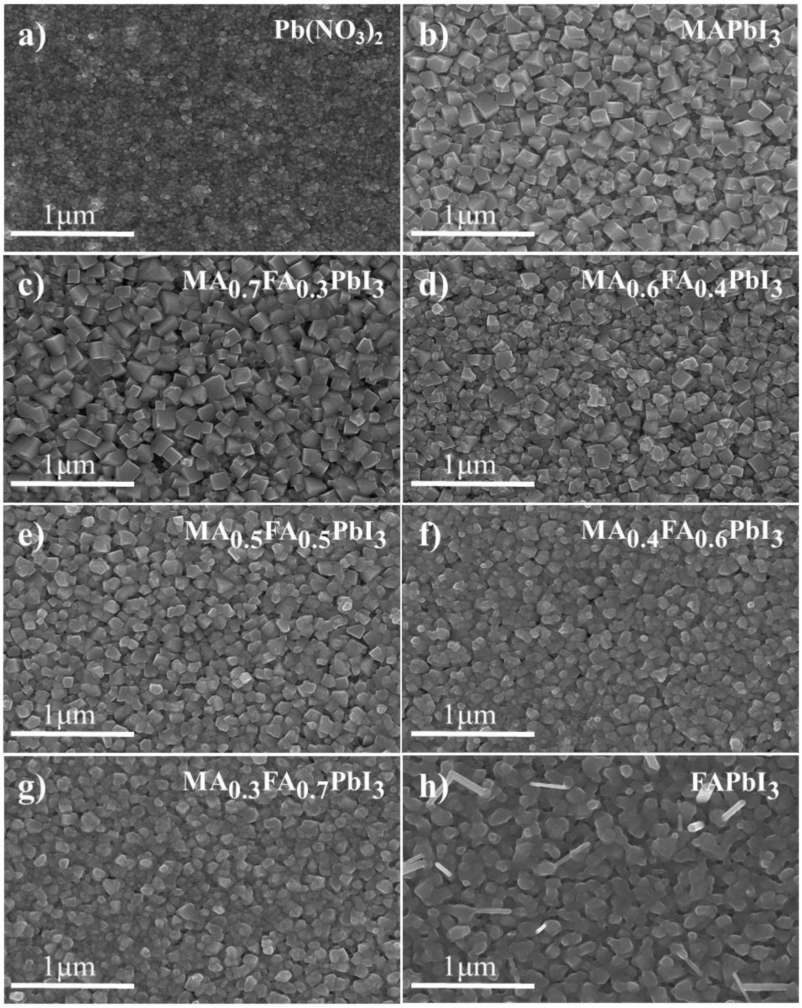

Figure 3. The FESEM surface morphologies of $MAPbI_3$, $FAPbI_3$ and $MA_xFA_{1-x}PbI_3$ perovskite films converted from (a) $Pb(NO_3)_2$ film adsorbed on ZnO/c-TiO_2/FTO substrate with (b) MAI, MAI/FAI mixed solutions with various molar ratios ((c) 0.7/0.3, (d) 0.6/0.4, (e) 0.5/0.5, (f) 0.4/0.6, and (g) 0.3/0.7), and (h) FAI by all simple dip-coating approach.

The $Pb(NO_3)_2$ film were readily prepared by dipping the ZnO/c-TiO_2/FTO substrate into an aqueous halide-free $Pb(NO_3)_2$ precursor solution, ensuring the particulate morphology with superior surface coverages as shown in Figure 3a. The stable $MAPbI_3$, $FAPbI_3$ and $MA_xFA_{1-x}PbI_3$ perovskite films were prepared via simple all-dip-coating deposition along-with the successful SSIER approach with this $Pb(NO_3)_2$ layer. These perovskite films originated mainly from $Pb(NO_3)_2$ particulate and the formed surface crystallinity possess sub-micron sized crystals with good surface topology on ZnO/c-TiO_2/FTO. These formed morphologies helps for an efficient charge transportation and have ability to suppress interfacial recombination between the electron transporting layer (ETL) and hole transporting layer (HTL), contemplating an efficient device performances of PrSCs. Particularly, we realized that their grain size and grain boundaries were mainly affected by the dipping solution condition such as cationic species or molar ratios of M[21]AI/FAI as shown in Figure 3b-h. Also, the dip-coating processed $FAPbI_3$ exhibited the larger grain size than that of $MAPbI_3$ films, and the lower composition of FAI in MAI/FAI solution leads to the more cubic-like crystal structures of $MA_xFA_{1-x}PbI_3$ perovskite films providing turbid and non-uniform absorption behavior by light scattering in the UV-Vis absorption spectra as shown in Figure 2a. Moreover, the rod-like structures which was attributed mainly as photo-inactive hexagonal δ-phase were partially observed in dip-coating processed $FAPbI_3$ films, they were not detected in $MA_xFA_{1-x}PbI_3$ perovskite films. These note that the MAI/FAI mixed composition can significantly affect to the cubic α-phase growth preferred thermodynamically in the $FAPbI_3$ perovskite crystallization. Thus, we characterized the crystallinity of perovskite structures via XRD patterns of the aforementioned $MA_xFA_{1-x}PbI_3$ films in which in which the FA and MA cations are simultaneously intercalated and compared to those of $MAPbI_3$ and $FAPbI_3$ films.[20]

Figure 4 shows (a) the XRD patterns of $MAPbI_3$, $FAPbI_3$ and $MA_xFA_{1-x}PbI_3$ films prepared on ZnO/c-TiO_2/FTO substrate with MAI (black), FAI (green), and MAI/FAI mixed solutions with various molar ratios (0.7/0.3 (blue), 0.6/0.4 (yellow), 0.5/0.5 (red), 0.4/0.6 (purple), and 0.3/0.7 (cyan)) by all simple dip-coating approach and (b) the correlated perovskite conversion factors. As shown in Figure 4a, these films presented usual XRD patterns of $MAPbI_3$ and α-$FAPbI_3$ crystalline structures with intense peaks at $2\theta = 14.2°$ and 13.8°, respectively relates to (001) diffraction planes.[2] The specific crystallinity peaks for PbI_2 and δ-$FAPbI_3$ (100) were observed at $2\theta = 12.7°$ and 11.8°, correspondingly. Interestingly, although dip-coating processed $FAPbI_3$ films obviously exhibited intense peaks of δ-$FAPbI_3$ (100) at $2\theta = 11.8°$ as well as α-$FAPbI_3$ (100) at $2\theta = 13.8°$, there is no any indication of δ-$FAPbI_3$ crystalline structures in XRD pattern of $MA_xFA_{1-x}PbI_3$ films.[21-22] These results could be well correlated with those observed in SEM surface morphologies of Figure 2. Moreover, we observed the diffraction peak shifting behavior at very small angles by increasing the FAI ratio in the MAI/FAI solutions. This might be caused by the lattice size of perovskite increased steadily by the large sized FA cation compared to MA cation.[22]

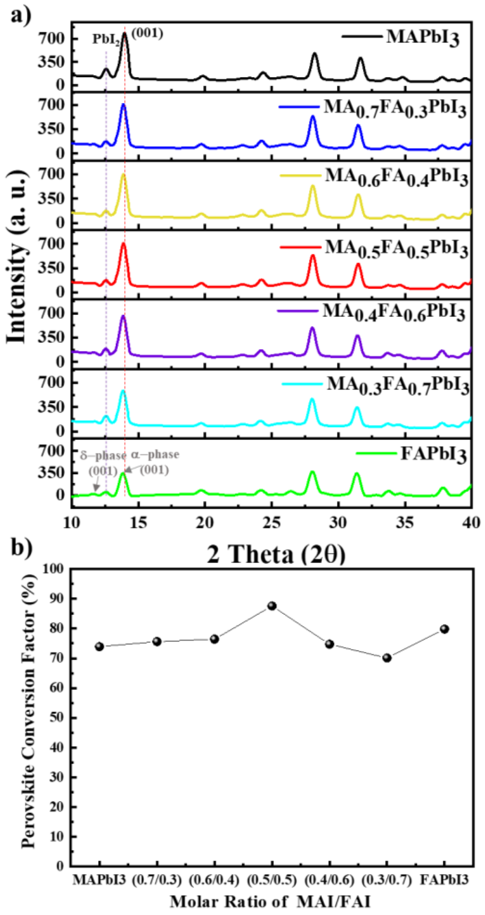

Figure 4. (a) the XRD patterns of $MAPbI_3$, $FAPbI_3$ and $MA_xFA_{1-x}PbI_3$ films prepared on ZnO/c-TiO_2/FTO substrate with MAI (black), FAI (green), and MAI/FAI mixed solutions with various molar ratios (0.7/0.3 (blue), 0.6/0.4 (yellow), 0.5/0.5 (red), 0.4/0.6 (purple), and 0.3/0.7 (cyan)) by all simple dip-coating approach and (b) the correlated perovskite conversion factors.

Based on these XRD patterns, we qualitatively evaluated the SSIER processed perovskite conversion factors (C_{MAPbI3}, C_{FAPbI3}, and $C_{MAxFA1-xPbI3}$) from PbI_2 intermediates into $MAPbI_3$, $FAPbI_3$, and $MA_xFA_{1-x}PbI_3$ perovskite structures, respectively by using peak intensities of PbI_2 and perovskites at $2\theta = 12.6°$ and 13.8°~14.02°, respectively.[15-20]

$$C_{perov} = I_{PbI2}/(I_{PbI2} + I_{perov}) \qquad (1)$$

As shown in Figure 4b, the perovskite conversion factor, C_{perov} values were significantly affected by the dipping solution condition such as cationic species or molar ratios of MAI/FAI. The $MA_{0.5}FA_{0.5}PbI_3$ perovskite film exhibited the higher conversion value compared to those of $MAPbI_3$, $FAPbI_3$, and other $MA_xFA_{1-x}PbI_3$ perovskites. These results indicate that the competitive insertion between MA and FA cations in perovskite crystal lattice might be closely correlated with the composition ratio in MAI/FAI mixed solution, affecting to perovskite crystal growth kinetics.[21-23]

Afterward, we investigated the efficient photovoltaic device performances for PrSCs with the aforementioned $MAPbI_3$, $FAPbI_3$, and $MA_xFA_{1-x}PbI_3$ perovskites sequentially deposited from aqueous $Pb(NO_3)_2$. The n-i-p type PHJ configuration of FTO/c-TiO_2/ZnO/Perovskite/HTM/MoO_3/Ag was fabricated. The relative conductivity as well as efficiency of the used HTM (spiro-OMeTAD) were boosted by doping with different additives like Li-TFSI and *t*-BPy. Figure 5 shows (a) the current-voltage (*J–V*) curves under an AM 1.5 irradiation (100 $mW{\cdot}cm^{-1}$) for the efficiently fabricated $MAPbI_3$, $FAPbI_3$, and $MA_xFA_{1-x}PbI_3$ perovskite layers fabricated with MAI (black), FAI (green), and five MAI/FAI mixed solutions (0.7/0.3 (blue), 0.6/0.4 (yellow), 0.5/0.5 (red), 0.4/0.6 (purple), and 0.3/0.7 (cyan)) and (b) the hysteresis behavior of the *J–V* curves for the PrSCs devices fabricated with the $MA_{0.5}FA_{0.5}PbI_3$ perovskites. The evaluation for photovoltaic performances of the fabricated devices in optimized fabrication condition was proceeded by evaluating more than 200 individual PrSCs devices. The obtained device performances distribution during these processes are showed in Figure S1-S7 and the efficient device performances in each condition are also summarized in Table S1.

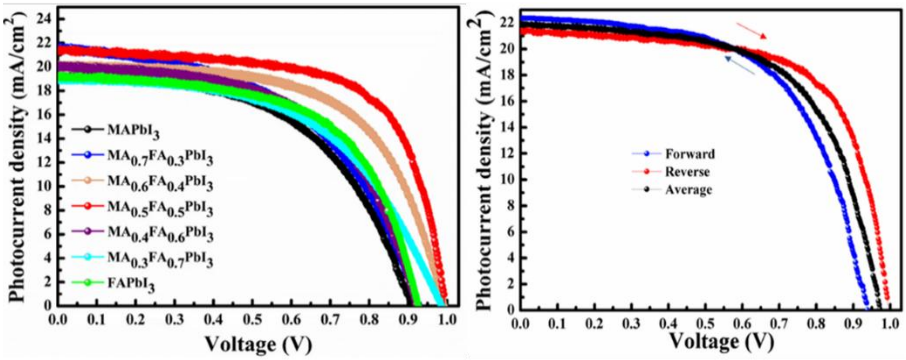

Figure 5. (a) the current-voltage (*J–V*) curves under an AM 1.5 irradiation (100 mW·cm^{-1}) for most efficient PrSCs based on $MAPbI_3$, $FAPbI_3$, and $MA_xFA_{1-x}PbI_3$ perovskite layers fabricated with MAI (black dotted line), FAI (green dotted line), and five MAI/FAI mixed solutions (0.7/0.3 (blue dotted line), 0.6/0.4 (yellow dotted line), 0.5/0.5 (red dotted line), 0.4/0.6 (purple dotted line), and 0.3/0.7 (cyan dotted line)) and (b) the hysteresis behavior of the *J–V* curves in both scan directions for the PrSCs devices fabricated with the $MA_{0.5}FA_{0.5}PbI_3$ perovskite layer.

As shown in Figure 5a, we have realized efficient device performances for PrSCs for the very first time with dip-all-coated processed $MA_{0.5}FA_{0.5}PbI_3$ perovskites and the PCE values are pretty notable with a maximum/average of 14.1%/13.69% with a J_{sc} of 21.2 mA·cm^{-2}, open-circuit voltage (V_{oc}) of 0.99

V, and fill factor (*F.F*) of 0.67. These values exhibited much better performance in-contrast to $MAPbI_3$ and $FAPbI_3$ devices carried out under the same conditions; the PCEs of 9.30%/9.07% (with J_{sc} = 19.24 mA·cm^{-2}, V_{oc} = 0.87 V, and *F.F* = 0.56) and 10.81%/10.72% (with J_{sc} = 19.09 mA·cm^{-2}, V_{oc} = 0.93 V, and *F.F* = 0.61), respectively. These outcomes might be because of the high perovskite conversion factors, superior surface morphology, and better crystallinity due to photo-inactive constituents such as PbI_2 and δ-$FAPbI_3$ in perovskite layers which may hindered efficient charge transportations.[24] The PrSCs devices with $MA_{0.7}FA_{0.3}PbI_3$, $MA_{0.6}FA_{0.4}PbI_3$, $MA_{0.4}FA_{0.6}PbI_3$, and $MA_{0.3}FA_{0.7}PbI_3$ perovskite layers also showed the efficient PCEs of 10.1%/9.61% (with J_{sc} = 21.5 mA·cm^{-2}, V_{oc} = 0.93 V, and *F.F* = 0.50), 12.42%/12.20% (with J_{sc} = 19.16 mA·cm^{-2}, V_{oc} = 1.01 V, and *F.F* = 0.64), 10.37%/10.09% (with J_{sc} = 19.98 mA·cm^{-2}, V_{oc} = 0.92 V, and *F.F* = 0.56), and 10.1%/9.72% (with J_{sc} = 19.1 mA·cm^{-2}, V_{oc} = 0.99V, and *F.F* = 0.53), respectively. While, the *J-V* hysteretic behaviour mainly depends on the scan directions and often showed in a typical n-i-p type PrSC devices mainly while using TiO_2 electrode due to various charge extraction as well as charge transportation rates of electrons and holes parted from the excitons.[25] As shown in Figure 5b, the PrSCs presented minor differences with deviation in J_{sc} values, whereas, V_{oc} and *F.F* values reduced slightly in the forward direction. However, the average PCE calculated in both directions is approximately 5% lowered than that obtained in the reverse direction.. These results might be caused by interfacial recombination with the TiO_2 electrode and due to the impurity issues of PbI_2, grain boundary, and a little pin-holes observed in surface coverage of perovskite film.[15-20]

Figure 6 shows (a) EQE and (b) the operational stability for the best-performing PrSC device with $MA_{0.5}FA_{0.5}PbI_3$ perovskite layer prepared by a sequential dip-coating approach. The stability of the champion devices was calculated without any encapsulation under N_2 atmosphere. As shown in Figure 6, the PrSC devices with $MA_{0.5}FA_{0.5}PbI_3$ perovskite layer presented good EQEs in their light-absorption area, where integrated photo-current correlates well with the J_{sc} values and also exhibited an outstanding operational stability without any noticeable lowering of photo-voltaic performances for 400 h.

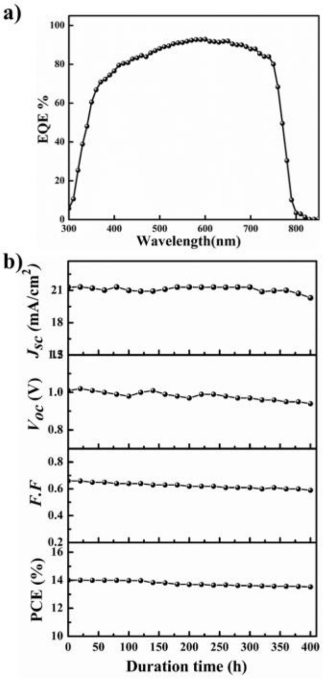

Figure 6. (a) EQE and (b) the operational stability for the best-performing PrSC device (under N_2 atmosphere) with $MA_{0.5}FA_{0.5}PbI_3$ perovskite layer prepared by a sequential dip-coating approach.

Conclusion

In summary, we have efficiently presented a simple preparation of highly efficient mixed cationic lead halide, $MA_xFA_{1-x}PbI_3$ perovskite films by employing all-sequential dip-coating deposition from aqueous lead precursor to develop the facile and environmentally friendly approaches for high-efficiency PrSCs. In this study, we modulated the dipping solution condition such as cationic species such as MAI and FAI or molar ratios of MAI/FAI mixture. The $MA_xFA_{1-x}PbI_3$ perovskite films prepared from MA and FA mixed cationic ligand coordination exhibited better characteristics compared to those of $MAPbI_3$ and $FAPbI_3$ with MA and FA ligand, respectively carried out under the same conditions. The high crystal conversion and growth factors from precursor, surface morphology and crystallinity were demonstrated in the $MA_xFA_{1-x}PbI_3$ perovskite films. Also, since the most efficient characteristics of perovskite films were mainly observed in $MA_{0.5}FA_{0.5}PbI_3$ perovskite films, we speculated that the competitive insertion the competitive insertion between MA and FA cations in perovskite crystal lattice might be closely correlated with the composition ratio in MAI/FAI mixed solution. Moreover, the outstanding device performances with improved stability with a PCE of ~14.1% in PrSC devices with the all-dip-coating processed $MA_{0.5}FA_{0.5}PbI_3$ perovskite layer. These results let us believe that this all-dip-coating process might add a good significance to the development and the fascinating deposition technology of perovskite film to dominate the spin-coating strategy which has a size restriction and the use of very toxic and detrimental organic solvents for highly performing PrSCs.

Chapter 5

Conclusion of the Study

Conclusion

We have demonstrated the preparation of highly efficient $FAPbI_3$ and $MA_xFA_{1-x}PbI_3$ perovskite materials using a simple, sequential all-dip-coating deposition in an aqueous nonhalide lead precursor solution and in pure FAI,MAI and FAI/MAI mixed solution toward a facile, cost-effective, and environmentally benign manufacturing processe for high-efficiency PrSCs. The $FAPbI_3$ and $MA_xFA_{1-x}PbI_3$ perovskite layers deposited via this dip-coating process The $MA_xFA_{1-x}PbI_3$ perovskite films prepared from MA and FA mixed cationic ligand coordination exhibited better characteristics compared to those of $MAPbI_3$ and $FAPbI_3$ with MA and FA ligand, respectively carried out under the same conditions. The high crystal conversion and growth factors from precursor, surface morphology and crystallinity were demonstrated in the $MA_xFA_{1-x}PbI_3$ perovskite films. Also, since the most efficient characteristics of perovskite films were mainly observed in $MA_{0.5}FA_{0.5}PbI_3$ perovskite films, we speculated that the competitive insertion the competitive insertion between MA and FA cations in perovskite crystal lattice might be closely correlated with the composition ratio in MAI/FAI mixed solution. Moreover, the outstanding device performances with improved stability with a PCE of ~14.1% in PrSC devices with the all-dip-coating processed $MA_{0.5}FA_{0.5}PbI_3$ perovskite layer. Thus, we successfully realized highly efficient $MAPbI_{3-x}Cl_x$ perovskite materials with an aqueous nonhalide lead precursor, in contrast to the conventional spin-casting approach that requires toxic organic solvents.

References

(1) Hao, F., et al., *Lead-Free Solid-State Organic–Inorganic Halide Perovskite Solar Cells*. Nature Photonics, 2014. **8** (6): p. 489–494.

(2) Colella, S., et al., *MAPbI3-XClx Mixed Halide Perovskite for Hybrid Solar Cells: The Role of Chloride as Dopant on the Transport and Structural Properties*. Chemistry of Materials, 2013. **25** (22): p. 4613–4618.

(3) Chen, C.-W., et al., *Efficient and Uniform Planar-Type Perovskite Solar Cells by Simple Sequential Vacuum Deposition.* Advanced materials (Deerfield Beach, Fla.), 2014. **26** (38): p. 6647–6652.

(4) Tavakoli, M.M., et al., *Large-Grain Tin-Rich Perovskite Films for Efficient Solar Cells via Metal Alloying Technique*. Advanced Materials, 2018. **30** (11): p. 1705998.

(5) Eames, C., et al., *Ionic Transport in Hybrid Lead Iodide Perovskite Solar Cells*. Nature Communications, 2015. **6** (1): p. 7497.

(6) Chen, C., et al., *Efficient Perovskite Solar Cells Based on Low-Temperature Solution-Processed (CH3NH3) PbI3 Perovskite/CuInS2 Planar Heterojunctions*. Nanoscale research letters, 2014. **9**: p. 457.

(7) Pellet, N., et al., *Mixed-Organic-Cation Perovskite Photovoltaics for Enhanced Solar-Light Harvesting*. Angewandte Chemie International Edition, 2014. **53** (12): p. 3151–3157.

(8) Tenuta, E., et al., *Thermodynamic Origin of Instability in Hybrid Halide Perovskites*. Scientific Reports, 2016**. 6** (1): p. 37654.

(9) Chen, Q., et al., *Planar Heterojunction Perovskite Solar Cells via Vapor-Assisted Solution Process*. Journal of the American Chemical Society, 2014**. 136** (2): p. 622–625.

(10) Niu, G., et al., *Study on the Stability of CH3NH3PbI3 Films and the Effect of Post-Modification by Aluminum Oxide in All-Solid-State Hybrid Solar Cells*. Journal of Materials Chemistry A, 2014**. 2** (3): p. 705–710.

(11) Hao, F., et al., *Anomalous Band Gap Behavior in Mixed Sn and Pb Perovskites Enables Broadening of Absorption Spectrum in Solar Cells*. Journal of the American Chemical Society, 2014**. 136** (22): p. 8094–8099.

(12) You, J., et al., *Low-Temperature Solution-Processed Perovskite Solar Cells with High Efficiency and Flexibility*. ACS Nano, 2014**. 8** (2): p. 1674–1680.

(13) Frecker, T., et al., *Review—Quantum Dots and Their Application in Lighting, Displays, and Biology*. ECS Journal of Solid-State Science and Technology, 2016**. 5**: p. R3019–R3031.

(14) Tidhar, Y., et al., *Crystallization of Methyl Ammonium Lead Halide Perovskites: Implications for Photovoltaic Applications*. Journal of the American Chemical Society, 2014**. 136** (38): p. 13249–13256.

(15) Wang, D., et al., *Reproducible One-Step Fabrication of Compact MAPbI3–XClx Thin Films Derived from Mixed-Lead-Halide Precursors*. Chemistry of Materials, 2014**. 26** (24): p. 7145–7150.

(16) Zong, Y., et al., *Homogenous Alloys of Formamidinium Lead Triiodide and Cesium Tin Triiodide for Efficient Ideal-Bandgap Perovskite Solar Cells*. Angewandte Chemie International Edition, 2017**. 56** (41): p. 12658–12662.

(17) Im, J.-H., et al., *Morphology-Photovoltaic Property Correlation in Perovskite Solar Cells: One-Step versus Two-Step Deposition of CH3NH3PbI3*. APL Materials, 2014**. 2** (8): p. 81510.

(18) Zhu, H.L., et al., *Controllable Crystallization of CH3NH3Sn0.25Pb0.75I3 Perovskites for Hysteresis-Free Solar Cells with Efficiency Reaching 15.2%*. Advanced Functional Materials, 2017**. 27** (11): p. 1605469.

(19) Wehrenfennig, C., et al., *High Charge Carrier Mobilities and Lifetimes in Organolead Trihalide Perovskites*. Advanced Materials, 2014**. 26** (10): p. 1584–1589.

(20) Dharani, S., et al., *High Efficiency Electrospun TiO2 Nanofiber Based Hybrid Organic–Inorganic Perovskite Solar Cell*. Nanoscale, 2014**. 6** (3): p. 1675–1679.

(21) Hu, L., et al., *Sequential Deposition of CH3NH3PbI3 on Planar NiO Film for Efficient Planar Perovskite Solar Cells*. ACS Photonics, 2014**. 1** (7): p. 547–553.

(22) Etgar, L., *Mesoscopic CH3NH3PbI3/TiO2 Heterojunction Solar Cells*. J. Am. Chem. Soc., 2012**. 134**: .

(23) McGehee, M.D., *Continuing to Soar*. Nature Materials, 2014**. 13** (9): p. 845–846.

(24) Eperon, G.E., et al., *Morphological Control for High Performance, Solution-Processed Planar Heterojunction Perovskite Solar Cells*. Advanced Functional Materials, 2014**. 24** (1): p. 151–157.

(25) Pang, S., et al., *NH2CH═NH2PbI3: An Alternative Organolead Iodide Perovskite Sensitizer for Mesoscopic Solar Cells*. Chemistry of Materials, 2014**. 26** (3): p. 1485–1491.

(26) Chen, H.-W., et al., *Emergence of Hysteresis and Transient Ferroelectric Response in Organo-Lead Halide Perovskite Solar Cells*. The Journal of Physical Chemistry Letters, 2015**. 6** (1): p. 164–169.

(27) Wei, J., et al., *Hysteresis Analysis Based on the Ferroelectric Effect in Hybrid Perovskite Solar Cells*. The Journal of Physical Chemistry Letters, 2014**. 5** (21): p. 3937–3945.

(28) Noel, N.K., et al., *Lead-Free Organic–Inorganic Tin Halide Perovskites for Photovoltaic Applications*. Energy & Environmental Science, 2014**. 7** (9): p. 3061–3068.

(29) Arora, N., et al., *Perovskite Solar Cells with CuSCN Hole Extraction Layers Yield Stabilized Efficiencies Greater than 20.* Science (New York, N.Y.), 2017**. 358** (6364): p. 768–771.

(30) Grancini, G., et al., *One-Year Stable Perovskite Solar Cells by 2D/3D Interface Engineering*. Nature Communications, 2017**. 8** (1): p. 15684.

(31) Christians, J.A., et al., *Best Practices in Perovskite Solar Cell Efficiency Measurements. Avoiding the Error of Making Bad Cells Look Good*. The Journal of Physical Chemistry Letters, 2015**. 6** (5): p. 852–857.

(32) Gong, J., et al., *Perovskite Photovoltaics: Life-Cycle Assessment of Energy and Environmental Impacts*. Energy & Environmental Science, 2015**. 8** (7): p. 1953–1968.

(33) Sepalage, G.A., et al., *Copper(I) Iodide as Hole-Conductor in Planar Perovskite Solar Cells: Probing the Origin of J–V Hysteresis*. Advanced Functional Materials, 2015**. 25** (35): p. 5650–5661.

(34) Ono, L.K., et al., *Temperature-Dependent Hysteresis Effects in Perovskite-Based Solar Cells*. Journal of Materials Chemistry A, 2015**. 3** (17): p. 9074–9080.

(35) Kim, H.-S., et al., *Parameters Affecting I-V Hysteresis of CH3NH3PbI3 Perovskite Solar Cells: Effects of Perovskite Crystal Size and Mesoporous TiO2 Layer*. The journal of physical chemistry letters, 2014**. 5** (17): p. 2927–2934.

(36) Li, C., et al., *Iodine Migration and Its Effect on Hysteresis in Perovskite Solar Cells*. Advanced Materials, 2016**. 28** (12): p. 2446–2454.

(37) Chapin, D.M., et al., *A New Silicon P‐ n Junction Photocell for Converting Solar Radiation into Electrical Power*. Journal of Applied Physics, 1954**. 25** (5): p. 676–677.

(38) Zhao, C., et al., *Revealing Underlying Processes Involved in Light Soaking Effects and Hysteresis Phenomena in Perovskite Solar Cells*. Advanced Energy Materials, 2015**. 5** (14): p. 1500279.

(39) Calado, P., et al., *Evidence for Ion Migration in Hybrid Perovskite Solar Cells with Minimal Hysteresis*. Nature Communications, 2016**. 7** (1): p. 13831.

(40) Meloni, S., et al., *Ionic Polarization-Induced Current–Voltage Hysteresis in CH3NH3PbX3 Perovskite Solar Cells*. Nature Communications, 2016**. 7** (1): p. 10334.

(41) Becquerel, A.E., *Recherches Sur Les Effets de La Radiation Chimique de La Lumiere Solaire Au Moyen Des Courants Electriques*. Comptes Rendus de L{\textasciiacute}Academie des Sciences, 1839**. 9**: p. 145–149.

(42) Sum, T.C., et al., *Advancements in Perovskite Solar Cells: Photophysics behind the Photovoltaics*. Energy Environ. Sci., 2014**. 7** (8): p. 2518–2534.

(43) Cheng, Y.-J., et al., *Synthesis of Conjugated Polymers for Organic Solar Cell Applications*. Chemical Reviews, 2009**. 109** (11): p. 5868–5923.

(44) Islam, M.B., et al., *Highly Stable Semi-Transparent MAPbI3 Perovskite Solar Cells with Operational Output for 4000 H*. Solar Energy Materials and Solar Cells, 2019**. 195**: p. 323–329.

(45) Wu, X., *High-Efficiency Polycrystalline CdTe Thin-Film Solar Cells*. Solar Energy, 2004**. 77**: p. 803–814.

(46) Sommeling, P.M., et al., *Long-Term Stability Testing of Dye-Sensitized Solar Cells*. Journal of Photochemistry and Photobiology A: Chemistry, 2004**. 164**: p. 137–144.

(47) Conibeer, G., *Third-Generation Photovoltaics*. Materials Today, 2007**. 10** (11): p. 42–50.

(48) Mathew, S., et al., *Dye-Sensitized Solar Cells with 13% Efficiency Achieved through the Molecular Engineering of Porphyrin Sensitizers.* Nature chemistry, 2014**. 6** (3): p. 242–247.

(49) Gong, J., et al., *Review on Dye-Sensitized Solar Cells (DSSCs): Advanced Techniques and Research Trends*. Renewable and Sustainable Energy Reviews, 2017**. 68**: p. 234–246.

(50) Snaith, H.J., *Perovskites: The Emergence of a New Era for Low-Cost, High-Efficiency Solar Cells*. The Journal of Physical Chemistry Letters, 2013**. 4** (21): p. 3623–3630.

(51) Grätzel, M., *Photoelectrochemical Cells.* Nature, 2001**. 414** (6861): p. 338–344.

(52) Dette, C., et al., *TiO2 Anatase with a Bandgap in the Visible Region.* Nano letters, 2014**. 14** (11): p. 6533–6538.

(53) Grossiord, N., et al., *Degradation Mechanisms in Organic Photovoltaic Devices*. Organic Electronics, 2012**. 13** (3): p. 432–456.

(54) Im, J.-H., et al., *6.5% Efficient Perovskite Quantum-Dot-Sensitized Solar Cell.* Nanoscale, 2011**. 3** (10): p. 4088–4093.

(55) Li, C., et al., *Formability of {\its ABX} ${\sb 3} $ ({\it X} = F, Cl, Br, I) Halide Perovskites*. Acta Crystallographica Section B, 2008**. 64** (6): p. 702–707.

(56) Park, N.-G., *Perovskite Solar Cells: An Emerging Photovoltaic Technology*. Materials Today, 2015**. 18** (2): p. 65–72.

(57) Upadhyaya, H.M., et al., *Recent Progress and the Status of Dye-Sensitised Solar Cell (DSSC) Technology with State-of-the-Art*

Conversion Efficiencies. Solar Energy Materials and Solar Cells, 2013**. 119**: p. 291–295.

(58) Etgar, L., *Mesoscopic CH3NH3PbI3/TiO2 Heterojunction Solar Cells*. J. Am. Chem. Soc., 2012**. 134**: .

(59) Fabregat-Santiago, F., et al., *Electron Transport and Recombination in Solid-State Dye Solar Cell with Spiro-OMeTAD as Hole Conductor*. Journal of the American Chemical Society, 2009**. 131** (2): p. 558–562.

(60) Snaith, H.J., et al., *Efficiency Enhancements in Solid-State Hybrid Solar Cells via Reduced Charge Recombination and Increased Light Capture.* Nano letters, 2007**. 7** (11): p. 3372–3376.

(61) Liu, M., *Efficient Planar Heterojunction Perovskite Solar Cells by Vapour Deposition*. Nature., 2013**. 501**:

(62) Liang, P., *Additive Enhanced Crystallization of Solution-Processed Perovskite for Highly Efficient Planar-Heterojunction Solar Cells*. Adv. Mater., 2014**. 26**.

(63) Snaith, H.J., *Anomalous Hysteresis in Perovskite Solar Cells*. J. Phys. Chem. Lett., 2014**. 5**.

(64) Lee, M.M., *Efficient Hybrid Solar Cells Based on Meso-Superstructured Organometal Halide Perovskites*. Science., 2012**. 338**.

(65) Kojima, A., *Organometal Halide Perovskites as Visible-Light Sensitizers for Photovoltaic Cells*. J. Am. Chem. Soc., 2009**. 131**.

(66) Juárez-Pérez, E.J., et al., *Perovskite Solar Cells Take a Step Forward*. Science, 2020**.** **368**: p. 1309.

(67) Xiao, Z., et al., *Efficient {,} High Yield Perovskite Photovoltaic Devices Grown by Interdiffusion of Solution-Processed Precursor Stacking Layers*. Energy Environ. Sci., 2014**.** **7** (8): p. 2619–2623.

(68) Saliba, M., et al., *Cesium-Containing Triple Cation Perovskite Solar Cells: Improved Stability, Reproducibility and High Efficiency*. Energy and Environmental Science, 2016**.** **9** (6): p. 1989–1997.

(69) Jeon, N.J., et al., *Solvent Engineering for High-Performance Inorganic-Organic Hybrid Perovskite Solar Cells*. Nature Materials, 2014**.** **13** (9): p. 897–903.

(70) Unger, E.L., et al., *Hysteresis and Transient Behavior in Current-Voltage Measurements of Hybrid-Perovskite Absorber Solar Cells*. Energy and Environmental Science, 2014**.** **7** (11): p. 3690–3698.

(71) Alcocer, M.J.P., et al., *Electron-Hole Diffusion Lengths Exceeding Trihalide Perovskite Absorber*. Science, 2013**.** **342** (October): p. 341–344.

(72) Jäger-Waldau, A., et al., *{PV} Status Report 2017 Study.*; 2017.

(73) Khenkin, M. V., et al., *Consensus Statement for Stability Assessment and Reporting for Perovskite Photovoltaics Based on ISOS Procedures*. Nature Energy, 2020**.** **5** (1): p. 35–49.

(74) Cheacharoen, R., et al., *Encapsulating Perovskite Solar Cells to Withstand Damp Heat and Thermal Cycling*. Sustainable Energy and Fuels, 2018**. 2** (11): p. 2398–2406.

(75) Bin, H., et al., *11.4% Efficiency Non-Fullerene Polymer Solar Cells with Trialkylsilyl Substituted 2D-Conjugated Polymer as Donor*. Nature Communications, 2016**. 7** (May): p. 1–11.

(76) Green, M., et al., *Solar Cell Efficiency Tables (Version 40)*. Ieee Trans Fuzzy Syst, 2012**. 20** (6): p. 1114–1129.

(77) Fthenakis, V., *Sustainability of Photovoltaics: The Case for Thin-Film Solar Cells*. Renewable and Sustainable Energy Reviews, 2009**. 13** (9): p. 2746–2750.

(78) Kazim, S., et al., *Perovskite as Light Harvester: A Game Changer in Photovoltaics*. Angewandte Chemie - International Edition, 2014**. 53** (11): p. 2812–2824.

(79) Green, M.A., et al., *Solar Cell Efficiency Tables (Version 51)*. Progress in Photovoltaics: Research and Applications, 2018**. 26** (1): p. 3–12.

(80) Sanehira, E.M., et al., *Enhanced Mobility CsPbI3 Quantum Dot Arrays for Record-Efficiency, High-Voltage Photovoltaic Cells*. Science Advances, 2017**. 3** (10).

(81) Snaith, H.J., et al., *Advances in Liquid-Electrolyte and Solid-State Dye-Sensitized Solar Cells*. Advanced Materials, 2007**. 19** (20): p. 3187–3200.

(82) Bisquert, J., et al., *The Causes of Degradation of Perovskite Solar Cells*. Journal of Physical Chemistry Letters, 2019**. 10** (19): p. 5889–5891.

(83) EPKI, *Perovskite-Based Photovoltaics: A Unique Chance for European PV-Industry*. White Paper from the EPKI, 2019**.** No. September.

(84) Shi, L., et al., *Gas Chromatography-Mass Spectrometry Analyses of Encapsulated Stable Perovskite Solar Cells*. Science, 2020**. 368** (6497).

(85) Kim, H.S., et al., *Lead Iodide Perovskite Sensitized All-Solid-State Submicron Thin Film Mesoscopic Solar Cell with Efficiency Exceeding 9%*. Scientific Reports, 2012**. 2**: p. 1–7.

(86) Burschka, J., et al., *Sequential Deposition as a Route to High-Performance Perovskite-Sensitized Solar Cells*. Nature, 2013**. 499** (7458): p. 316–319.

(87) Xiao, Z., et al., *Efficient {,} High Yield Perovskite Photovoltaic Devices Grown by Interdiffusion of Solution-Processed Precursor Stacking Layers*. Energy Environ. Sci., 2014**. 7** (8): p. 2619–2623.

(88) Unger, E.L., et al., *Hysteresis and Transient Behavior in Current-Voltage Measurements of Hybrid-Perovskite Absorber Solar Cells*. Energy and Environmental Science, 2014**. 7** (11): p. 3690–3698.

(89) Song, X., et al., *Additive to Regulate the Perovskite Crystal Film Growth in Planar Heterojunction Solar Cells*. Applied Physics Letters, 2015**. 106** (3): p. 33901.

(89) Akin, S., et al., *New strategies for defect passivation in high‐ efficiency perovskite solar cells*. Advanced Energy Materials, 2020. **10**(13), p.1903090.

(90) Liu, Y., et al., *Ultrahydrophobic 3D/2D fluoroarene bilayer-based water-resistant perovskite solar cells with efficiencies exceeding 22%.* Science advances, 2019.***5***(6), p.2543.

(91) Seo, J.Y., et al., *Novel p-dopant toward highly efficient and stable perovskite solar cells*. Energy & Environmental Science, 2018 *11***(10)**, pp.2985-2992.

(92) Sahli, F., et al., *Fully textured monolithic perovskite/silicon tandem solar cells with 25.2% power conversion efficiency*. Nature materials, 2018.17**(9),** pp.820-826.

(93) Adnan, M. and Lee, J.K., *Highly efficient planar heterojunction perovskite solar cells with sequentially dip-coated deposited perovskite layers from a non-halide aqueous lead precursor*. RSC Advances, 2020. 10**(9),** pp.5454-5461.

(94) Adnan, M. and Lee, J.K., *All sequential dip-coating processed perovskite layers from an aqueous lead precursor for high efficiency perovskite solar cells*. Scientific reports, 2018. 8**(1),** pp.1-10.

(95) Adnan, M., et al., *Facile all-dip-coating deposition of highly efficient (CH 3) 3 NPbI 3− x Cl x perovskite materials from aqueous non-halide lead precursor*. RSC Advances, 2020. 10**(48)**, pp.29010-29017.

(96) Irshad, Z., et al., *Efficient Planar Heterojunction Inverted Perovskite Solar Cells with Perovskite Materials Deposited Using an Aqueous Non‐ Halide Lead Precursor*. Bulletin of the Korean Chemical Society, 2020. 41**(9),** pp.937-942.

(97) Akin, S., et al., *Cesiumlead based inorganic perovskite quantum-dots as interfacial layer for highly stable perovskite solar cells with exceeding 21% efficiency*. Nano Energy, 2019. **60**, pp.557-566.

(98) Leijtens, T., et al., *Stability of metal halide perovskite solar cells*. Advanced Energy Materials, 2015. 5 **(20),** p.1500963.

(99) Adnan, M., et al., *Efficient Synthesis and Characterization of Solvatochromic Fluorophore*. Bulletin of the Korean Chemical Society, 2017. 38 **(9),** pp.1052-1057.

(100) Jeon, N.J., et al., *Compositional engineering of perovskite materials for high-performance solar cells*. Nature, 2015. 517 **(7535),** pp.476-480.

(101) Zhang, Y., et al., *Achieving reproducible and high-efficiency (> 21%) perovskite solar cells with a presynthesized FAPbI3 powder*. ACS Energy Letters, 2019. 5 **(2),** pp.360-366.

(102) Akin, S., Akman, E. and Sonmezoglu, S., *FAPbI3‐ Based Perovskite Solar Cells Employing Hexyl‐ Based Ionic Liquid with an Efficiency Over 20% and Excellent Long‐ Term Stability*. Advanced Functional Materials, 2020. 30 **(28)**, p.2002964.

(103) Jeon, N.J., et al., *A fluorene-terminated hole-transporting material for highly efficient and stable perovskite solar cells*. Nature Energy, 2018. 3 **(8),** pp.682-689.

(104) Jeon, N.J., et al., *A fluorene-terminated hole-transporting material for highly efficient and stable perovskite solar cells*. Nature Energy, 2018. 3 **(8),** pp.682-689.

(105) Lee, J.W., et al., *High‐ efficiency perovskite solar cells based on the black polymorph of HC (NH2) 2PbI3*. Advanced Materials, 2014. 26 **(29),** pp.4991-4998.

(106) Niu, T., et al, *High performance ambient-air-stable FAPbI 3 perovskite solar cells with molecule-passivated Ruddlesden–Popper/3D heterostructured film*. Energy & Environmental Science, 2018. 11 **(12),** pp.3358-3366.

(107) Yuan, J., et al., *Two-dimensional perovskite capping layer for stable and efficient tin-lead perovskite solar cells*. Science China Chemistry, 2019. 62 **(5)**, pp.629-636.

(108) Wu, C., et al., *FAPbI3 flexible solar cells with a record efficiency of 19.38% fabricated in air via ligand and additive synergetic process*. Advanced Functional Materials, 2019. 29 **(34),** p.1902974.

(109) Prathapani, et al., *Experimental evaluation of room temperature crystallization and phase evolution of hybrid perovskite materials*. CrystEngComm, 2017. 19 **(27),** pp.3834-3843.

(110) Zhang, M., et al., *High-performance photodiode-type photodetectors based on polycrystalline formamidinium lead iodide perovskite thin films*. Scientific reports, 2018. 8 **(1),** pp.1-9.

(111) Fu, Y., et al., *Nanowire lasers of formamidinium lead halide perovskites and their stabilized alloys with improved stability*. Nano letters, 2016. 16 **(2),** pp.1000-1008.

(112) Zhang, Y., et al., *Efficient inverted planar formamidinium lead iodide perovskite solar cells via a post improved perovskite layer*. Rsc Advances, 2016 *6* **(83),** pp.79952-79957.

(113) Seol, D.J et al., *On the role of interfaces in planar- structured HC (NH2) 2PbI3 perovskite solar cells*. ChemSusChem, 2015. 8 **(14),** pp.2414-2419.

(114) Xu, X., et al., *Highly efficient planar perovskite solar cells with a TiO 2/ZnO electron transport bilayer*. Journal of Materials Chemistry A, 2015. 3 **(38),** pp.19288-19293.

(115) Hsieh, T.Y., et al., *Efficient perovskite solar cells fabricated using an aqueous lead nitrate precursor*. Chemical Communications, 2015. 51 **(68),** pp.13294-13297.

(116) Xu, X., et al., *Highly efficient planar perovskite solar cells with a TiO 2/ZnO electron transport bilayer*. Journal of Materials Chemistry A, 2015. 3 **(38),** pp.19288-19293.

(117) Yang, Z., et al., *Effects of formamidinium and bromide ion substitution in methylammonium lead triiodide toward high-performance perovskite solar cells*. Nano Energy, 2016. **22**, pp.328-337.

(118) Chen, J., et al., *Mixed-Organic-Cation (FA) x (MA) 1–x PbI3 Planar Perovskite Solar Cells with 16.48% Efficiency via a Low-Pressure Vapor-Assisted Solution Process*. ACS applied materials & interfaces, 2017 9 **(3),** pp.2449-2458.

(119) Zhao, Y.L., et al., *Fabrication of mixed perovskite organic cation thin films via controllable cation exchange*. Chinese Physics B, 2018 27 **(2),** p.024208.

(120) Aharon, S., et al., *Temperature dependence of hole conductor free formamidinium lead iodide perovskite based solar cells*. Journal of Materials Chemistry A, 2015. 3 **(17),** pp.9171-9178.

(121) Xiao, M., Zhao, et al., *Application of mixed-organic-cation for high performance hole-conductor-free perovskite solar cells*. Journal of colloid and interface science, 2018. **510**, pp.118-126.

(122) Salado, M., et al., *Influence of the mixed organic cation ratio in lead iodide based perovskite on the performance of solar cells*. Physical Chemistry Chemical Physics, 2016. 18 **(39),** pp.27148-27157.

(123) Piatkowski, P., er al., *Unraveling charge carriers generation, diffusion, and recombination in formamidinium lead triiodide perovskite polycrystalline thin film*. The journal of physical chemistry letters, 2016. 7 **(1),** pp.204-210.

(124) Han, Q., et al., *Single crystal formamidinium lead iodide (FAPbI3): insight into the structural, optical, and electrical properties*. Advanced Materials, 2016. 28 **(11),** pp.2253-2258.

(125) Zhang, Y., et al., *Optimization of stable quasi-cubic FA x MA1–x PbI3 perovskite structure for solar cells with efficiency beyond 20%*. ACS Energy Letters, 2017. 2 **(4),** pp.802-806.

(126) Gélvez-Rueda, M.C., et al., *Temperature dependent charge carrier dynamics in formamidinium lead iodide perovskite*. The Journal of Physical Chemistry C, 2017. 121 **(42),** pp.23392-23397.

(127) Aguiar, J.A., et al.,. *In situ investigation of the formation and metastability of formamidinium lead tri-iodide perovskite solar cells*. Energy & Environmental Science, 2016 9 **(7),** pp.2372-2382.

(128) Eperon, G.E., et al., *Cation exchange for thin film lead iodide perovskite interconversion.* Materials Horizons, 2016. 3 **(1),** pp.63-71.

(129) Smecca, E., et al., *Stability of solution-processed MAPbI 3 and FAPbI 3 layers.* Physical Chemistry Chemical Physics, 2016. 18 **(19),** pp.13413-13422.

(130) Irshad, Z., et al., *Controlling phase and morphology of all-dip-coating processed HC (NH2) 2PbI3 perovskite layers from an aqueous halide-free lead precursor*. Journal of Physics and Chemistry of Solids, 2022. **160**, p.110374.

(131) Gordillo-Guzmán, G., et al., *Synthesis and optimization of properties of thin films of FAx (MA1-X) PbI3 grown by spin coating with perovskite structure to be used as active layer in hybrid solar cells*. Revista UIS Ingenierías, 2020. 19 **(1),** pp.87-94.

(132) Slimi, B., et al., *Perovskite FA1-xMAxPbI3 for solar cells: films formation and properties*. Energy Procedia, 2016. **102**, pp.87-95.

(133) Huang, Y., Li, L et al, *The intrinsic properties of FA (1− x) MA x PbI 3 perovskite single crystals*. Journal of Materials Chemistry A, 2017. 5 **(18)**, pp.8537-8544.

(134) Unger, E.L., et al., *Hysteresis and transient behavior in current–voltage measurements of hybrid-perovskite absorber solar cells.* Energy & Environmental Science, 2014. 7 **(11),** pp.3690-3698.

Appendix A

Acknowledgement

First and foremost, I would like to express my sincere gratitude to my advisor **Prof. Jae Kwan Lee** for his guidance and motivation. I can't thank him enough for providing me the great opportunity to pursue my Ph.D. under his supervision. He has been a marvelous mentor to me. I'm grateful for his continuous support, patience and sharing of his immense research knowledge and ideas with me. I always enjoyed the lab meetings and the discussion time with him and have learned a lot from him. His teaching and expertise have made my Ph.D. experience productive and interesting. As my advisor, his understanding and care for me made my tough times in the Ph.D. manageable. His advice on both research as well as on my career have been priceless. Throughout my Ph.D., he gave me the moral support and the freedom to pursue the research I wanted to do. Without his guidance and constant feedback, this Ph.D. would not have been possible.

My sincere thanks to the thesis committee members: 김호중, 손홍래, 이재관, 김선우, 김용인 for evaluating my thesis. Their insightful comments and questions have made my defense enjoyable and memorable.

I owe my gratitude to Chosun University International office team for their academic help in various stages of my Ph.D. They took us on field trips to various parts of Korea which helped me to understand and embrace the culture of Korea and warm gesture of Korean people. I thank the former coordinator

Yushin Jeong and current coordinator **Mr. Ji Hongbum** for all their help and kindness and constant feedback throughout my Ph.D. study.

Words cannot express my thankfulness to **my parents**. They raised me independently and allowed to decide my career and pursue towards it. I also thank my sisters, my daughter **Miraal Adnan** and my husband **Muhammad Adnan** for all their encouragement and support.

My deep appreciation goes to my senior **Mr. Kyeong Kuk Koh** who have been supportive in many ways. There are innumerable situations we discussed our research and worked together all night to keep up with deadline. I am also grateful to my lab mate **Muhammad Adnan** for her help and wonderful fun lab time. The time we spent together will always be remembered and cherished.

Besides my lab members, I extend my sincere gratitude to my all **Chosun University** friends (**Mr. Umar Afzaal, Mr. Waqas Elahi, Mr. Waleed Hussain Siddique, Dr. Swapnil Bhujbal, Mr. Hasanul Banna** and **Miss Isabel** for their help and moral support. My special thanks to my brothers **Adeel Anjum and Humayun Hassan** for their constant support throughout my Ph.D. journey.

Last but not least, I would like to thank all of my friends from Pakistan for their constant encouragement. My special thanks to my uncles **Mr. Altaf Hussain** and **Dr. Riaz Hussain and in-laws** for their constant support, this journey was not possible without their kind attention. Following this, my special gratitude to my ex-professor **Dr. Javed Iqbal** for his countless help and guiding throughout my Master to Ph.D. journey. Also, my special thanks to **Sundas jamil, Misbha usman, Kalsoom,**

I thank everyone who helped directly and indirectly to complete my doctoral study successfully.

Appendix B

List of publications

1. **Irshad, Z**., Adnan M, & Lee, J. K. (2022). Controlling phase and morphology of all-dip-coating processed HC (NH2) 2PbI3 perovskite layers from an aqueous halide-free lead precursor. Journal of Physics and Chemistry of Solids. 160, p.1103-74.

2. Adnan, M., **Irshad, Z**., & Lee, J. K. (2020). Facile all-dip-coating deposition of highly efficient (ch 3) 3 npbi3- x cl x perovskite materials from aqueous non-halide lead precursor. RSC Advances, 10(48), 29010–29017.

3. **Irshad, Z**., Adnan, M., & Lee, J. K. (2020). Efficient Planar Heterojunction Inverted Perovskite Solar Cells with Perovskite Materials Deposited Using an Aqueous Non-Halide Lead Precursor. Bulletin of the Korean Chemical Society, 41(9), 937-942.

4. . Bilal Ahmed Siddique, M., Hussain, R., Ali Siddique, S., Yasir Mehboob, M., **Irshad, Z**., Iqbal, J., & Adnan, M*. (2020a). Enhancement in photovoltaic properties of n, n-diethylaniline based donor materials by bridging core modifications for efficient solar cells. Chemistry Select, 5(25), 7358–7369.

5. Mehboob, M. Y., Khan, M. U., Hussain, R., Ayub, K., Sattar, A., Ahmad, M. K., **Irshad, Z.,** & Adnan, M*. (2020). Designing of benzodithiophene core-based small molecular acceptors for efficient non-fullerene organic solar cells. Spectrochimica Acta Part A: Molecular and Biomolecular Spectroscopy, 118873.

6. Siddique, S. A., Siddique, M. B. A., Hussain, R., Liu, X., Mehboob, Z., Muhammad Yasir and **Z. Irshad,** & Adnan, M*. (2020). Efficient tuning of triphenylamine-based donor materials for high-efficiency organic solar cells. Computational and Theoretical Chemistry, 113045.

7. Younas, F., Mehboob, M. Y., Ayub, K., Hussain, R., Umar, A., Khan, M. U., **Irshad, Z.**, & Adnan, M*. (2020). Efficient cu decorated inorganic b12p12 nanoclusters for sensing toxic cocl2 gas: A detailed DFT study. Journal of Computational Biophysics and Chemistry.

8. Hussain, R., Yasir Mehboob, M., Usman Khan, M., Khalid, M., **Irshad, Z**., Fatima, R., Anwar, A., Nawab, S., & Adnan, M*****. (2020). Efficient designing of triphenylamine based hole transport materials with outstanding photovoltaic characteristics for organic solar cells. Journal of Materials Science, 1–19.

I dedicate this thesis to my family and friends who believed in me to achieve my dream. Their unconditional love, constant support and grace has always kept me going.